AGU PUBLICATIONS

JGR

Journal of Geophysical Research: Oceans

RESEARCH ARTICLE

10.1002/2015JC010751

Key Points:
- RSOW is identified with low PV and high CFC-12 and SF6
- RSOW is formed through mixed-layer deepening in winter in the northern Red Sea
- Eddies can cause significant stirring and mixing

Correspondence to:
P. Zhai,
pingzhai425@gmail.com

Citation:
Zhai, P., A. S. Bower, W. M. Smethie, and L. J. Pratt (2015), Formation and spreading of Red Sea Outflow Water in the Red Sea, *J. Geophys. Res. Oceans*, *120*, 6542–6563, doi:10.1002/2015JC010751.

Received 26 JAN 2015
Accepted 7 SEP 2015
Accepted article online 10 SEP 2015
Published online 29 SEP 2015

Formation and spreading of Red Sea Outflow Water in the Red Sea

Ping Zhai[1,2], Amy S. Bower[3], William M. Smethie Jr.[4], and Larry J. Pratt[3]

[1]MIT-WHOI Joint Program in Physical Oceanography, Woods Hole Oceanographic Institution, Woods Hole, Massachusetts, USA, [2]Now at Department of Marine, Earth and Atmospheric Sciences, North Carolina State University, Raleigh, North Carolina, USA, [3]Department of Physical Oceanography, Woods Hole Oceanographic Institution, Woods Hole, Massachusetts, USA, [4]Lamont-Doherty Earth Observatory of Columbia University, Palisades, New York, USA

Abstract Hydrographic data, chlorofluorocarbon-12 (CFC-12) and sulfur hexafluoride (SF_6) measurements collected in March 2010 and September–October 2011 in the Red Sea, as well as an idealized numerical experiment are used to study the formation and spreading of Red Sea Outflow Water (RSOW) in the Red Sea. Analysis of inert tracers, potential vorticity distributions, and model results confirm that RSOW is formed through mixed-layer deepening caused by sea surface buoyancy loss in winter in the northern Red Sea and reveal more details on RSOW spreading rates, pathways, and vertical structure. The southward spreading of RSOW after its formation is identified as a layer with minimum potential vorticity and maximum CFC-12 and SF_6. Ventilation ages of seawater within the RSOW layer, calculated from the partial pressure of SF_6 (pSF_6), range from 2 years in the northern Red Sea to 15 years at 17°N. The distribution of the tracer ages is in agreement with the model circulation field which shows a rapid transport of RSOW from its formation region to the southern Red Sea where there are longer circulation pathways and hence longer residence time due to basin wide eddies. The mean residence time of RSOW within the Red Sea estimated from the pSF_6 age is 4.7 years. This time scale is very close to the mean transit time (4.8 years) for particles from the RSOW formation region to reach the exit at the Strait of Bab el Mandeb in the numerical experiment.

1. Introduction and Background

The Red Sea is a semienclosed marginal sea, connected to the Indian Ocean via the narrow, shallow Strait of Bab el Mandeb (Figure 1). It presents many of the same features as other marginal seas, such as the Mediterranean Sea. These regions are characterized by net buoyancy loss from the ocean to the atmosphere due to heat flux, freshwater flux, or both. Buoyancy loss over marginal seas can produce dense intermediate and deep water masses, which feed the deep branch of the global thermohaline circulation. These water masses usually have distinct water properties.

Due to high evaporation, negligible precipitation, and no river runoff, the Red Sea is one of the most saline ocean basins in the world. As summarized in *Sofianos et al*. [2002], previous studies estimate that the annual mean heat and freshwater losses to the atmosphere over the Red Sea range from 1 to 75 W m^{-2} and 1.5 to 3.5 m yr^{-1}. Heat and freshwater fluxes over the Red Sea must be balanced by heat and freshwater transports through the Strait of Bab el Mandeb to maintain a steady state. Using this constraint, combined with current and water property data measured at the Strait of Bab el Mandeb, *Sofianos et al*. [2002] estimate that the annual mean heat and freshwater losses to the atmosphere are 11 ± 5 W m^{-2} and 2.06 ± 0.22 m yr^{-1}, respectively. The Red Sea Outflow Water (RSOW), which is formed in the northern Red Sea due to surface buoyancy loss, is one of the most saline water masses in the world ocean. After flowing over the 137 m deep Hanish Sill, RSOW entrains less dense overlying water in the Gulf of Aden and its properties change dramatically. With a combination of observational data and numerical simulations, *Bower et al*. [2000, 2005] found that RSOW reached neutral buoyancy at about 400–800 m in the Gulf of Aden with a salinity of 37.5. After significant mixing due to mesoscale eddy activity in the Gulf of Aden [*Bower and Furey*, 2011], RSOW moves southward along the African coast and through the Mozambique Channel [*Wyrtki*, 1973; *Beal et al*., 2000]. RSOW has been observed in the Agulhas retroflection region, up to 6000 km away from its source, as a water mass with high salinity and low oxygen at intermediate depth [*Gordon et al*., 1987; *Valentine et al*., 1993; *Beal et al*., 2000]. By using a simple mixing model, *Beal et al*. [2000]

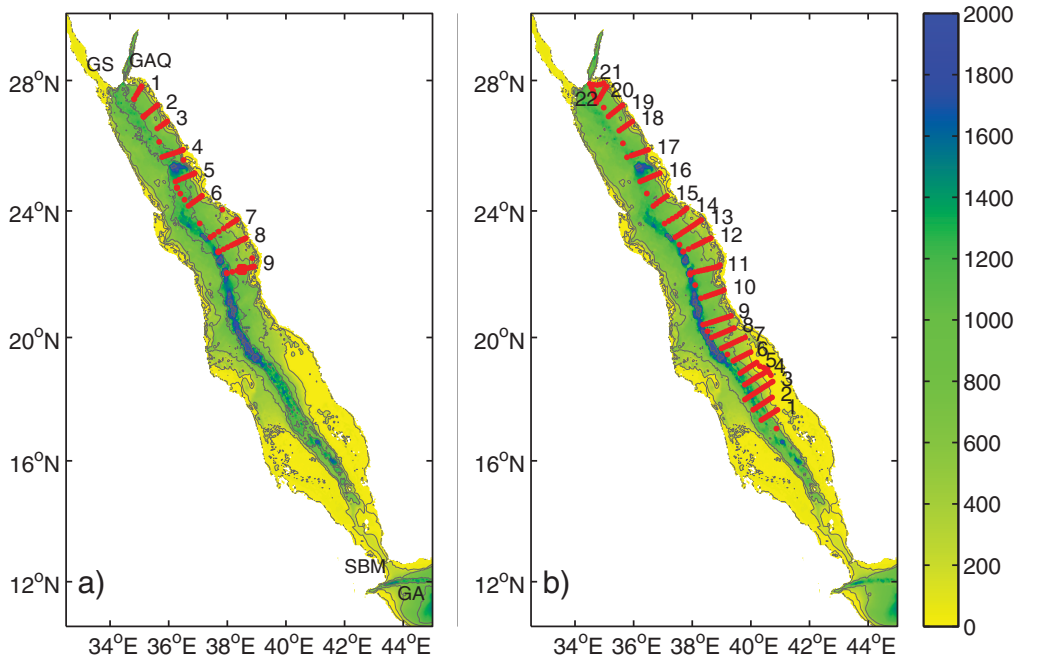

Figure 1. Locations of CTD stations and transects (numbers) of Red Sea cruises during (a) March 2010 and (b) September–October 2011. Colors represent bathymetry (m). The locations of Gulf of Aqaba (GAQ), Gulf of Suez (GS), Gulf of Aden (GA), and Strait of Bab el Mandeb (SBM) are shown in Figure 1a.

suggested that RSOW dominates the Indian Ocean salt budget in the intermediate-depth layer. RSOW can also be used as a tracer to investigate the Indian Ocean circulation. Therefore, studying the formation mechanism and properties of RSOW in the Red Sea is important in understanding RSOW's impact on Indian Ocean circulation and properties.

Previous observations in the Strait of Bab el Mandeb [e.g., *Morcos*, 1970; *Maillard and Soliman*, 1986; *Patzert*, 1974; *Neumann and McGill*, 1962; *Murray and Johns*, 1997; *Smeed*, 2004] indicate a two-layer exchange flow pattern in winter (November through March) and a three-layer exchange flow pattern in summer (June through September). In the winter season, RSOW with a salinity of ~40 flows out of the Red Sea beneath an incoming surface layer from the Gulf of Aden that has a salinity of ~36.5. The summer structure includes a surface flow from the Red Sea, an intermediate intrusion of Gulf of Aden Intermediate Water (GAIW), and the outflowing RSOW at the bottom of the strait. An 18 month time series of moored ADCP and hydrographic observations of the exchange flow at the Strait of Bab el Mandeb was collected in 1995–1996 [*Murray and Johns*, 1997; *Sofianos et al.*, 2002]. Velocity data indicate that in winter the average transport of RSOW was 0.6 Sv, with a speed of 0.8–1 m s^{-1}. In summer, the mean RSOW transport was reduced to 0.05 Sv, with a speed of 0.2–0.3 m s^{-1}.

The primary aim of this study is to improve the understanding of RSOW formation and its spreading pathways in the Red Sea. Section 2 introduces the data sets used in this study. The formation of RSOW is described in section 3. In section 4, potential vorticity (PV), chlorofluorocarbon-12 (CFC-12), and sulfur hexafluoride (SF_6) distributions are used to identify the recently ventilated RSOW in the Red Sea. Section 5 describes the spreading pathways and transit times of the RSOW calculated from an idealized numerical model. Section 6 contains conclusions and a discussion.

2. Data Description

2.1. Hydrographic and CFC-12/SF_6 Data

Two hydrographic survey cruises were conducted in the Red Sea from the *R/V Aegaeo* during 16–29 March 2010 and 15 September to 10 October 2011 by the Woods Hole Oceanographic Institution and King

Abdullah University of Science and Technology. The primary purpose of these cruises was to carry out a large-scale survey of the eastern Red Sea, including observations of top-to-bottom ocean currents and temperature, salinity, dissolved oxygen, turbidity, and fluorescence. The cruise that was conducted in March 2010 consisted of 111 CTD (Conductivity, Temperature, and Depth) and LADCP (Lowered Acoustic Doppler Current Profiler) stations. The cruise in September and October 2011 consisted of 206 CTD and LADCP stations. Figure 1 shows the locations of CTD and LADCP stations for these two cruises. The station spacing along each transect was about 10 km. At each station, profiles of temperature, salinity, dissolved oxygen, and velocity data were collected using a modified SeaBird 911plus rosette/CTD system and upward and downward facing 300 kHz Workhorse LADCPs. Seawater samples were collected at nearly all stations to calibrate CTD measurements of salinity and oxygen. Velocity in the upper 600 m along the cruise track was also measured by a 75 kHz Ocean Surveyor shipboard ADCP (SADCP) mounted on the ship's hull. The potential temperature and salinity along the central axis of the Red Sea measured in the March 2010 and September–October 2011 cruises are shown in Figures 2 and 3. Potential temperature and salinity in the upper 200 m in the Red Sea vary in different seasons, while potential temperature and salinity below 200 m depth are nearly homogeneous. A less stratified layer between potential densities $27.5 < \sigma_\theta < 27.7$ kg m^{-3} was observed in March 2010. The potential temperature and salinity minima measured at the southernmost station in September–October 2011 are associated with GAIW, which flows from the Gulf of Aden into the Red Sea in summer. The GAIW with low potential temperature and salinity was also observed in summer 2002 [*Sofianos and Johns*, 2007].

Natural and anthropogenic tracers, such as ^{3}He, ^{14}C, CFCs, and SF_6, are frequently used in ocean circulation studies to define the circulation pathways, time scales, and transport of deep water masses. CFCs and SF_6 are trace gases of industrial origin that cause stratospheric ozone depletion and are also greenhouse gases. Release of CFCs into the atmosphere began in the 1940s, and their concentration in the atmosphere increased with time until the 1990s, when their use was curtailed by the Montreal Protocol. SF_6 has entered the atmosphere since the 1960s and is currently increasing at about 0.25 pptv per year (Figure 4). This nicely complements the CFCs input which leveled off in the 1990s. A small fraction of atmospheric CFCs and SF_6 enters the ocean through air-sea gas exchange at the ocean surface. They are chemically inert in seawater and are carried from the surface to the interior by currents and turbulent mixing. They can be used as an indicator of ocean ventilation and to determine the source of intermediate and deep water masses [*Mecking and Warner*, 2001; *Fine et al*., 2008; *Hartin et al*., 2011; *Smethie*, 1993; *Smethie et al*., 2000; *Schlosser et al*., 1991; *Willey et al*., 2004]. CFC measurements in the Gulf of Aden have been used to investigate ventilation of Red Sea Water [*Mecking and Warner*, 1999]. *Plähn et al*. [2002] analyzed CFC measurements in the far northern Red Sea to investigate the sources of Red Sea Deep Water (RSDW). During the September–October 2011 Red Sea cruise, water samples for CFC-12 and SF_6 analysis were collected at selected stations and returned to Lamont-Doherty Earth Observatory for measurement. Ground glass stoppered bottles with a volume of 250 mL were used to collect samples for CFC-12 and SF_6 with no head space at five stations, and 60 mL flame sealed glass ampoules were used to collect CFC-12 samples at 14 stations. The ampoules were flame sealed under continuously flowing nitrogen to keep the water samples from being contaminated by air and a correction based on CFC-12 solubility [*Warner and Weiss*, 1985] was made for CFC-12 in the nitrogen headspace. Both stoppered bottles and ampoules samples were collected at stations 194, 157, and 205 to compare the two sampling methods.

The error for CFC-12 measurements on flame sealed ampoule samples is typically $\pm$ the larger of 0.01 pmol kg^{-1} or 1% [*Mensch et al*., 1998] and the agreement between the ampoules and glass stoppered bottle measurements agree at this level. A comparison of pSF_6 (partial pressure of SF_6) and pCFC-12 (partial pressure of CFC-12) for the glass stoppered bottle samples suggest the SF_6 data for this cruise have an uncertainty of about $\pm$15–20%, which may be related to sample storage; the typical accuracy for SF_6 samples measured onboard ship is $\pm$2–4%. The locations of these samples are shown in Figure 5. The CFC-12 and SF_6 data obtained during the 2011 cruise were the first such data for the Red Sea between 17°N and 28°N.

2.2. Sea Surface Temperature

SST can be determined from satellite remote sensing using microwave (MW) and infrared (IR) radiometers. IR SST has higher spatial resolution (1–4 km) than MW SST (25 km). However, the accuracy of IR SST is affected by clouds. The advantage of MW radiometry is that it is not affected by cloud cover. In this study,

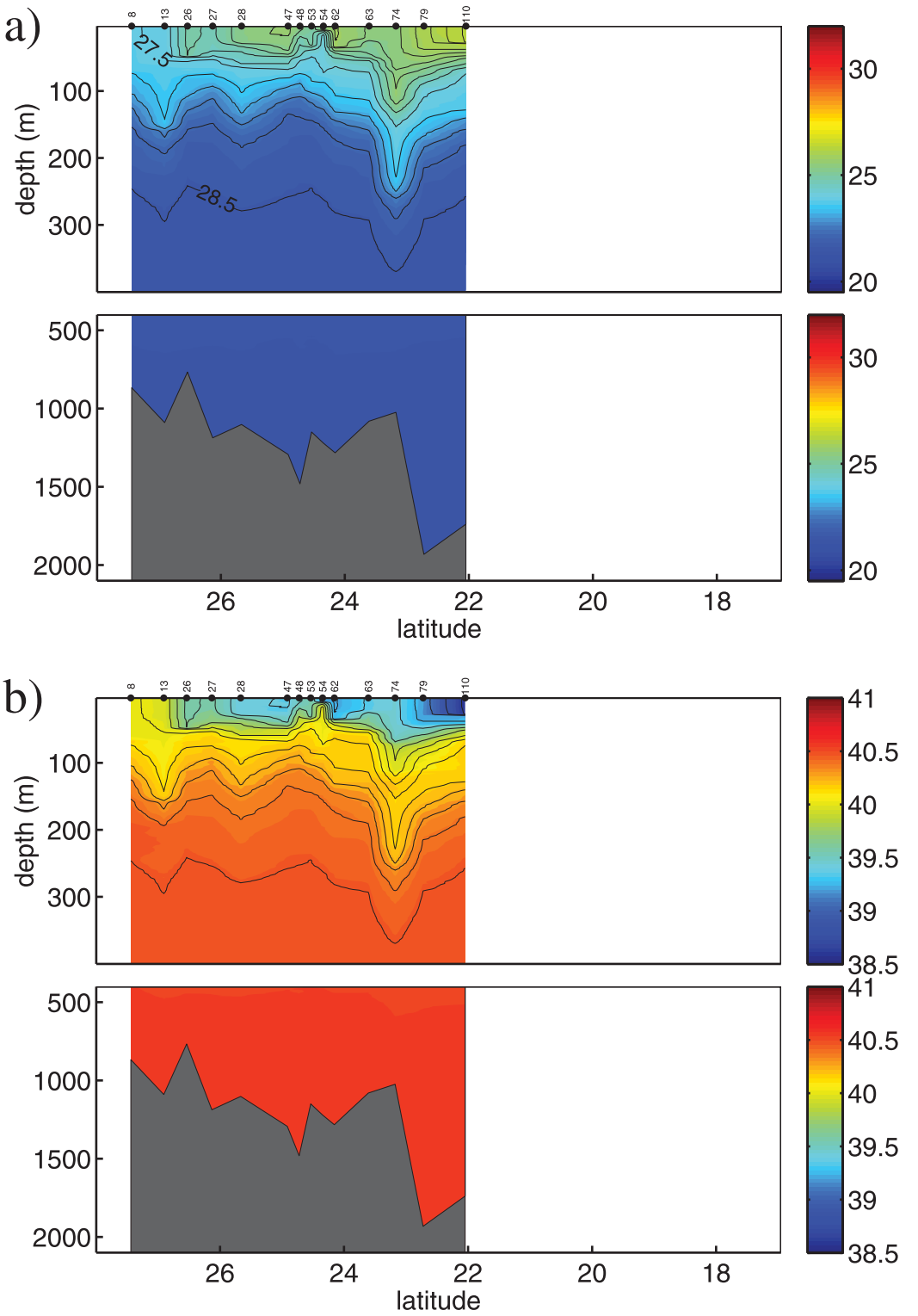

Figure 2. (a) Potential temperature (°C) and (b) salinity along the central axis of the Red Sea in March 2010 cruise. Black contours indicate potential density (contour interval is 0.2 kg m^{-3}). Stations along the axis are marked with black dots and station numbers.

we use MW-IR SST which is processed and distributed by Remote Sensing System (RSS). This product combines the satellite observations from MW and IR sensors. The MW SST is derived from the Advanced Microwave Scanning Radiometer (AMSR-E), the Tropical Rainfall Measuring Mission's Microwave Image (TMI), and

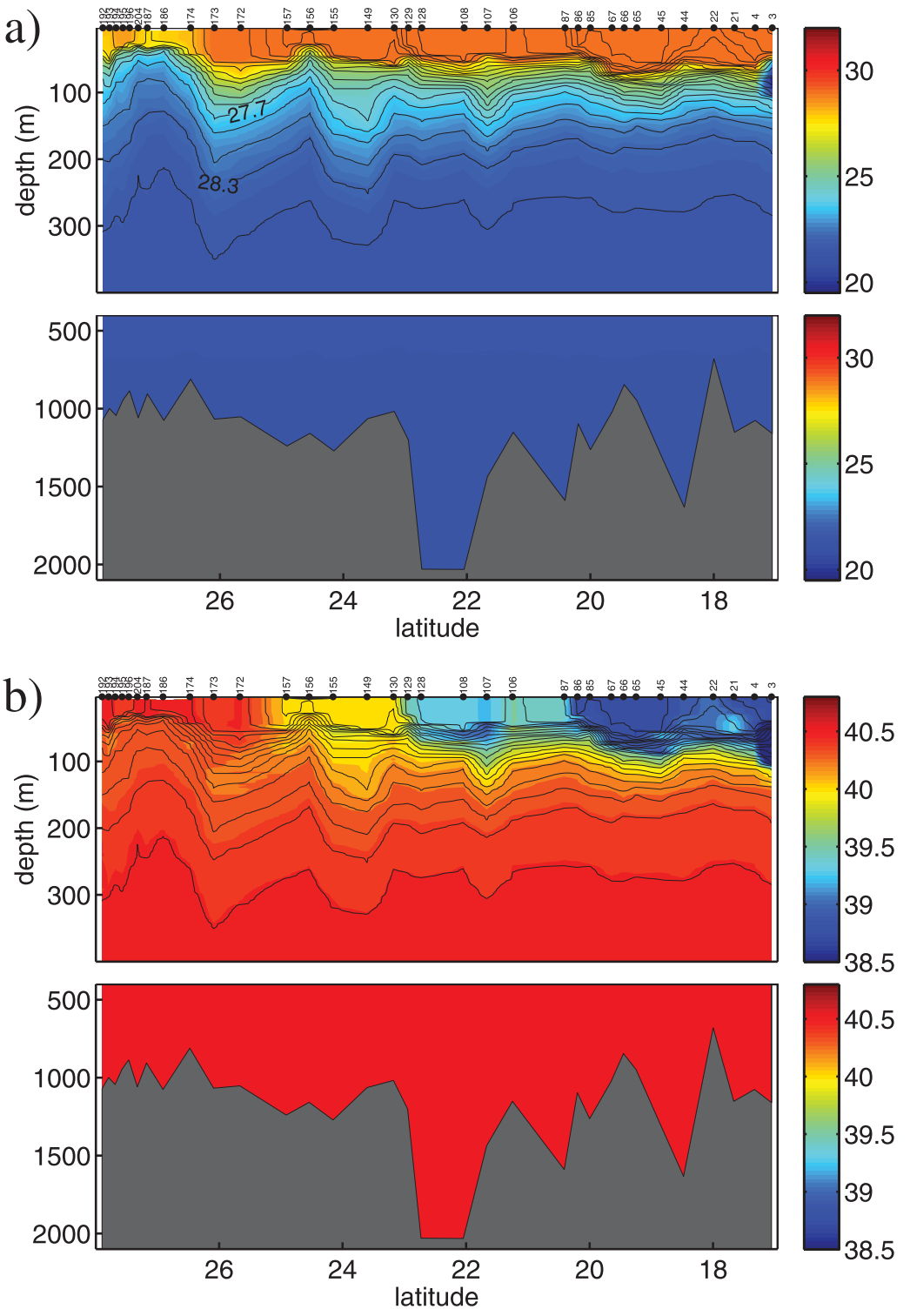

Figure 3. Same as Figure 2, but in September–October 2011 cruise.

the WindSAT Polarimetric Radiometer (WindSAT). The IR SST is derived from MODerate-resolution Imaging Spectroradiometer (MODIS). The merged MW-IR SST product has greater coverage and higher resolution than the SST product that is derived from MW or IR. The MW-IR SST product is distributed on a 0.09° grid from January 2006 (http://www.remss.com/measurements/sea-surface-temperature).

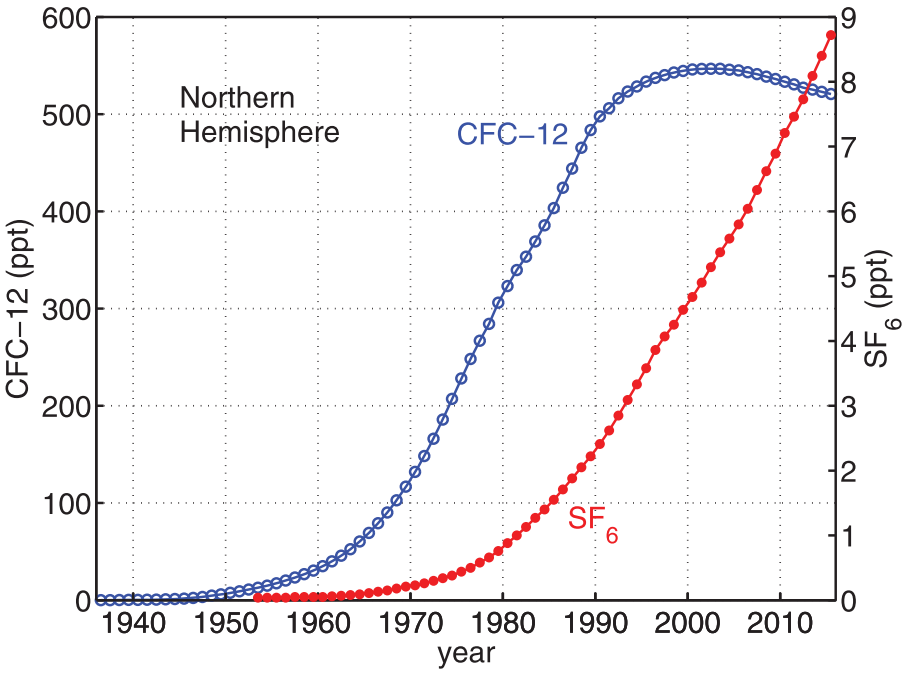

Figure 4. Concentrations of CFC-12 and SF_6 in the northern hemisphere atmosphere versus time.

2.3. Sea Surface Heat Flux

The sea surface heat flux used in this study is obtained from the global Objectively Analyzed air-sea Flux (OAflux). The OAflux is constructed from an objective analysis of in situ observations, satellite data, and atmospheric reanalysis [*Yu et al.*, 2008]. The fluxes are computed using the Coupled Ocean-Atmosphere Response Experiment (COARE) bulk flux algorithm 3.0 and are mapped on a regular 1° grid. The data product used in this study includes the monthly mean net heat flux and evaporation for the period from 1984 to 2009.

2.4. QuikSCAT and ASCAT Winds

The QuikSCAT (Quik Scatterometer) was launched in 1999 and its mission ended in November 2009. The QuikSCAT winds analyzed here are produced by Remote Sensing Systems and sponsored by the NASA Ocean Vector Winds Science Team. The QuikSCAT data product includes daily and time averaged wind data (3 day average, weekly, and monthly) at 10 m above the sea surface. The data product used here is 0.25° gridded data. An air-sea interaction buoy was deployed on 11 October 2008 at 22.16°N, 38.50°E in the Red Sea 60 km offshore of the Saudi Arabian coast. The QuikSCAT wind speeds compare well with the buoy wind measurements [*Zhai and Bower*, 2013]. Their results show that the mean differences for wind speed and direction are -0.02 m s^{-1} and 10.7°, root mean squared differences are 0.68 m s^{-1} and 29.9° and correlation coefficients of 0.95 and 0.76.

The Advanced Scatterometer (ASCAT) onboard Metop-A was launched in 2006 and provides sea surface wind at 10 m height since March 2007. The data product is mapped on a 0.25° grid. ASCAT wind has similar accuracies to QuikSCAT based on previous studies [*Bentamy et al.*, 2008]. Wind data before November 2009 used in this study are from QuikSCAT and data after November 2009 are from ASCAT.

3. Formation of RSOW in the Northern Red Sea

There are no direct observations to explore formation of RSOW in previous studies. What mechanisms are responsible for formation of RSOW are still open to debate. Using the Miami Isopycnic Coordinate Ocean Model (MICOM), *Sofianos and Johns* [2003] simulated the formation of RSOW. They suggested that RSOW was formed through open-ocean convection in the northern Red Sea, which was associated with a cyclonic

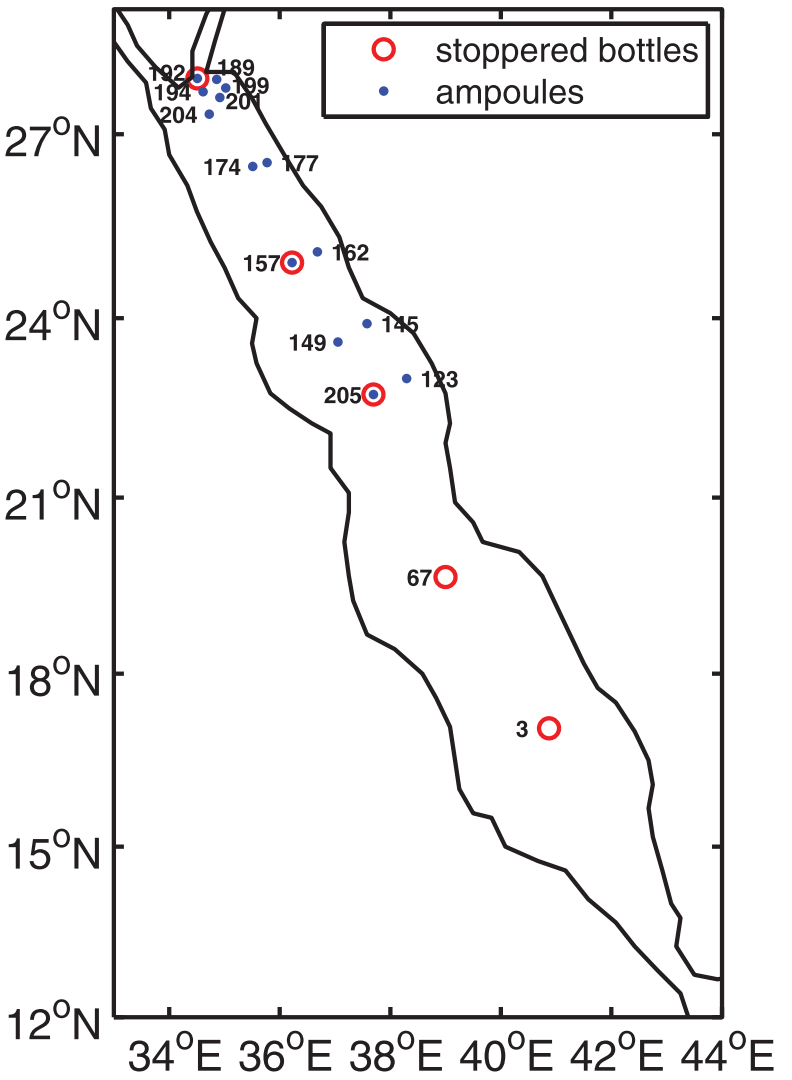

Figure 5. Station numbers and locations for CFC-12 and SF_6 water sample collection during 15 September 2011 to 10 October 2011 Red Sea cruise. SF_6 was measured only on the bottle samples; CFC-12 was measured on both bottle and ampoule samples.

gyre in that region. Some previous observations in the Red Sea suggest that there is a cyclonic gyre in the northern Red Sea which can bring the weakly stratified water close to surface in winter [*Morcos and Soliman*, 1974; *Clifford et al*., 1997; *Manasrah et al*., 2004; *Chen et al*., 2014; *Yao et al*., 2014]. The cyclonic gyre is also revealed in satellite SST images (Figure 6). However, the surface buoyancy loss in winter is not strong enough and the deepening of the mixed layer in winter to about 100–150 m in the northern Red Sea may not qualify as a deep convection event.

Deepening of mixed layers during wintertime surface buoyancy loss is one of the most important mechanisms of water mass formation in the global oceans, such as the formation of subtropical mode waters in the North Atlantic and North Pacific [*Hanawa and Talley*, 2001]. After formation of these mode waters in late winter, the surface water becomes restratified due to weakening of sea surface buoyancy loss. These mode waters are then capped by a seasonal pycnocline and advected away from their formation area. Mode waters are usually identified as a pycnostad layer with nearly homogeneous water properties. In Figure 2, a less stratified layer appears between potential densities $27.5 < \sigma_\theta < 27.7$ kg m^{-3}, which is in accordance with the density range of RSOW observed at the Strait of Bab el Mandeb [*Sofianos et al*., 2002]. Like the formation of mode waters, the formation of RSOW is also associated to deepening of mixed layer in winter which is caused by large negative oceanic heat flux to the atmosphere. The northern stations in Figure 2a captured surface densities belonging to the RSOW.

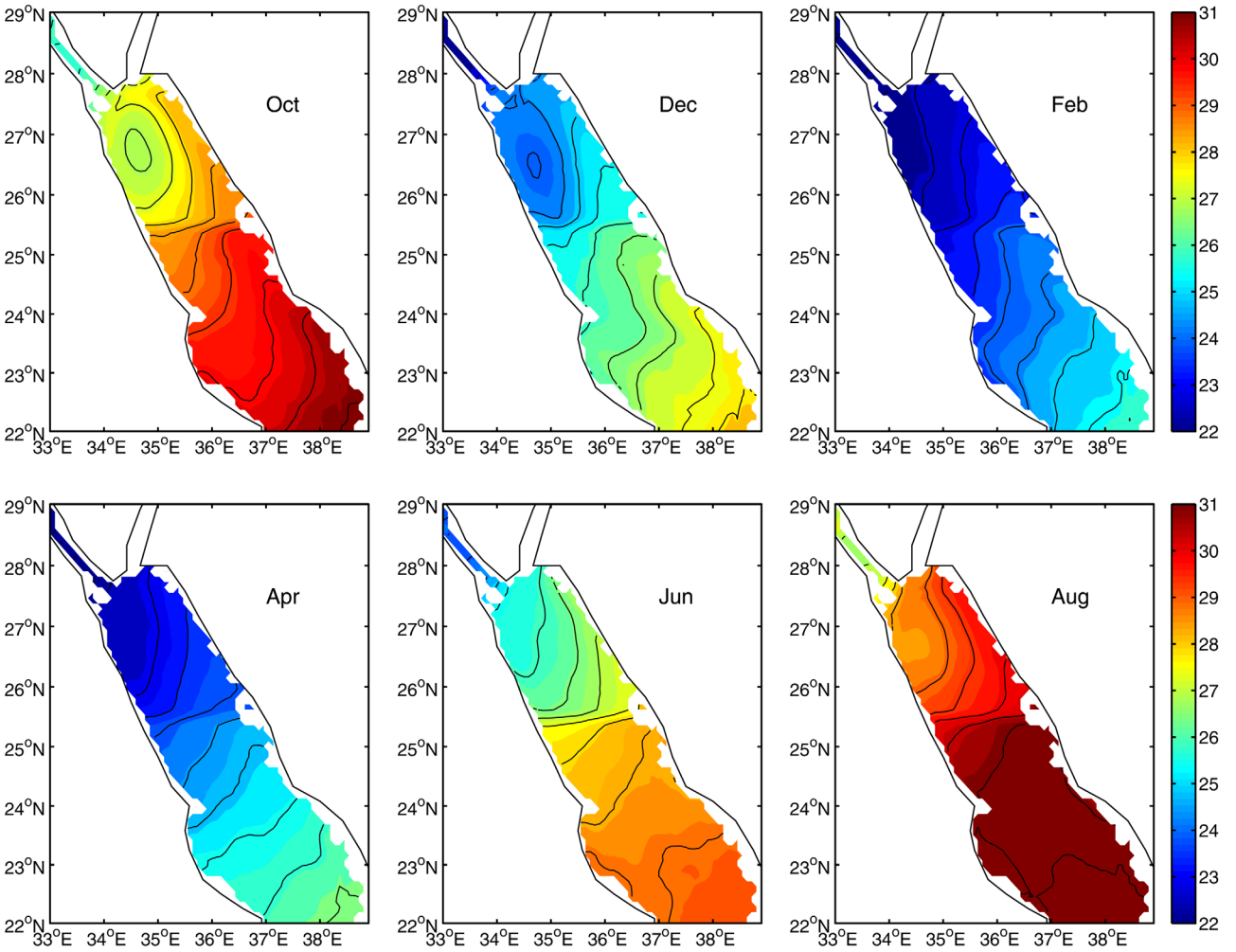

Figure 6. Monthly mean SST (contour interval = 0.5°C) in selected months. Monthly mean SST is obtained by averaging MW-IR SST from the years 2006 to 2012.

The air-sea buoyancy flux averaged north of 25°N has a strong seasonal cycle (Figure 7). The ocean loses heat to the atmosphere from September to March with peak heat loss of -200 W m^{-2} in January. By April, the sea surface buoyancy loss has stopped. *Papadopoulos et al.* [2013] found that the maximum turbulent heat loss in winter in the northern Red Sea varied from year to year. They pointed out that the extreme heat loss events in certain years were caused by positive sea level pressure (SLP) anomalies over the eastern Mediterranean and Middle East. In these years, strong southeastward wind carried cold and dry air into the northern Red Sea and led to extreme heat loss and evaporation. In accordance with the annual cycle of sea surface buoyancy flux, SST in the northern Red Sea also shows seasonal variations (Figure 6). After April, the surface buoyancy loss ceases, and the surface water becomes restratified. A well-mixed layer, the RSOW, remains as intermediate water below the surface and spreads out at its neutrally buoyant level (Figure 2).

Figure 6 reveals that the coldest water is located closer to the western part of the basin. The horizontal structure of surface 10 m winds indicates that the winds are stronger near the western boundary than that near the eastern boundary, likely leading to more evaporative cooling there (Figure 8). The Gulf of Suez and Gulf of Aqaba connect with the northern Red Sea and are surrounded by mountains. The surface winds in the two gulfs are mainly along the longitudinal axis of the basins due to the mountains' constraint. Winds from the Gulf of Suez and Gulf of Aqaba appear to converge near the western boundary of the northern Red Sea and cause stronger wind there. This idea is supported by a high-resolution numerical simulation using the Weather Research and Forecasting (WRF) model [*Jiang et al.*, 2009]. The WRF model was re-initialized every day with NCEP reanalysis, and then run forward at higher resolution. Their simulation

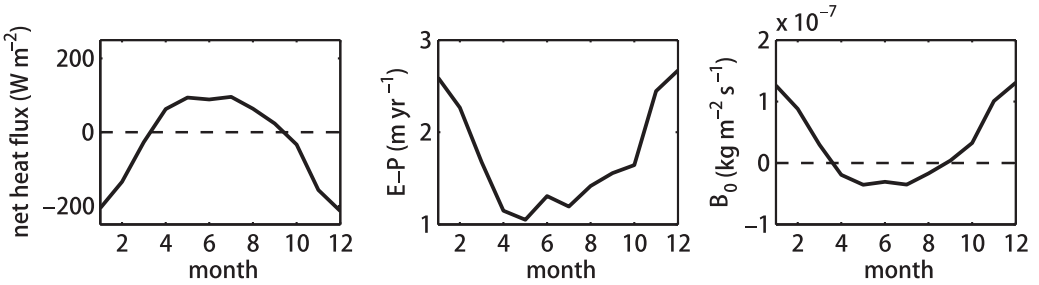

Figure 7. Mean annual cycle of net heat flux (W m^{-2}), evaporation rate (m yr^{-1}), and buoyancy flux (kg m^{-2} s^{-1}) averaged north of 25°N calculated from OAflux product. Buoyancy flux is calculated through $B_0 = -\alpha_T Q/c_w + \rho_0 \beta_S S_0 (E-P)$, where ρ_0, T_0, and S_0 are reference density, temperature, and salinity, respectively, $\alpha_T = 2\times10^{-4}$ °C^{-1} and $\beta_S = 8\times10^{-4}$ are thermal expansion and haline contraction coefficients, and $c_w = 3900$ J kg^{-1} °C^{-1} is the heat capacity of water.

captured the wind pattern in the Gulf of Suez and Gulf of Aqaba, which was not observed by QuikSCAT due to the narrow aspect ratio of these gulfs. The turbulent heat flux (including latent and sensible heat fluxes) and evaporation increase with wind speed. Therefore, wind can influence the surface temperature and salinity. The presence of stronger winds close to the western boundary might explain the asymmetry in the cold pool. However, we cannot confirm this with OAflux because of its coarse resolution. Western intensification due to β (meridional gradient of Coriolis parameter) might also contribute to the asymmetry in the cold pool, because doming in isopycnals, wherever produced, tends to propagate westward.

In summary, our study suggests that RSOW appears to be formed by mixed-layer deepening in winter time and then remains as a nearly homogeneous layer below the sea surface. Next we will show how this water mass is usually marked with distinct properties, such as low PV and high concentrations of CFC-12 and SF_6.

4. Observations of RSOW Spreading in the Red Sea

Only a few studies have addressed the southward spreading of RSOW after its formation [*Phillips*, 1966; *Cember*, 1988; *Sofianos and Johns*, 2003]. *Phillips* [1966] developed a two-dimensional similarity model to study buoyancy-driven circulation in the Red Sea. He pointed out that buoyancy loss over the Red Sea surface drove a shallow overturning circulation which included a northward surface current and a southward subsurface current. The southward flow returns to the Gulf of Aden through the Strait of Bab el Mandeb. Based on Carbon-14 and ^{3}He profiles at three stations along the middle axis of the Red Sea, *Cember* [1988] inferred a southward flowing current in about 100–200 m depth range. *Sofianos and Johns* [2003] simulated the formation and spreading of RSOW using the Miami Isopycnic Coordinate Ocean Model (MICOM). They found that RSOW was carried southward through the Red Sea by a southward flowing undercurrent, which was western intensified, after RSOW was formed in the northern Red Sea. *Yao et al.* [2014] explored the three-dimensional overturning circulation in the Red Sea using MITgcm with realistic topography and run over 50 years. Their numerical model results suggest that most of the southward transport of RSOW in the northern half of the Red Sea occurs along the western boundary which is consistent with our model simulation shown in the next section. These studies of southward spreading of RSOW are based on limited observations or numerical simulations. Here we will provide new evidence of the horizontal and vertical structure of RSOW spreading by analyzing hydrographic, CFC-12, and SF_6 data.

When mixed-layer deepening stops and the surface water starts to restratify in late winter, the recently formed RSOW with nearly homogeneous water properties (Figure 2) remains trapped below the surface and flows southward in a specific density range. The homogeneous layer signifies weak stratification and thus relatively low PV ($-f/\rho_0 \partial\rho/\partial z$). Figure 9 shows PV calculated from density profiles measured during the March 2010 cruise. The RSOW is identifiable by a minimum of PV which is bounded by isopycnals of 27.5 and 27.7 kg m^{-3}. The distribution of the minimum of PV layer compares well with the two bounded isopycnals. For example, at transect 7, the two isopycnals rise eastward in the same direction as the minimum of PV layer.

The PV minimum layer is less easily identifiable during the September–October 2011 cruise. Nine typical transects are selected to describe the PV structure (Figure 10). These sections represent PV distributions

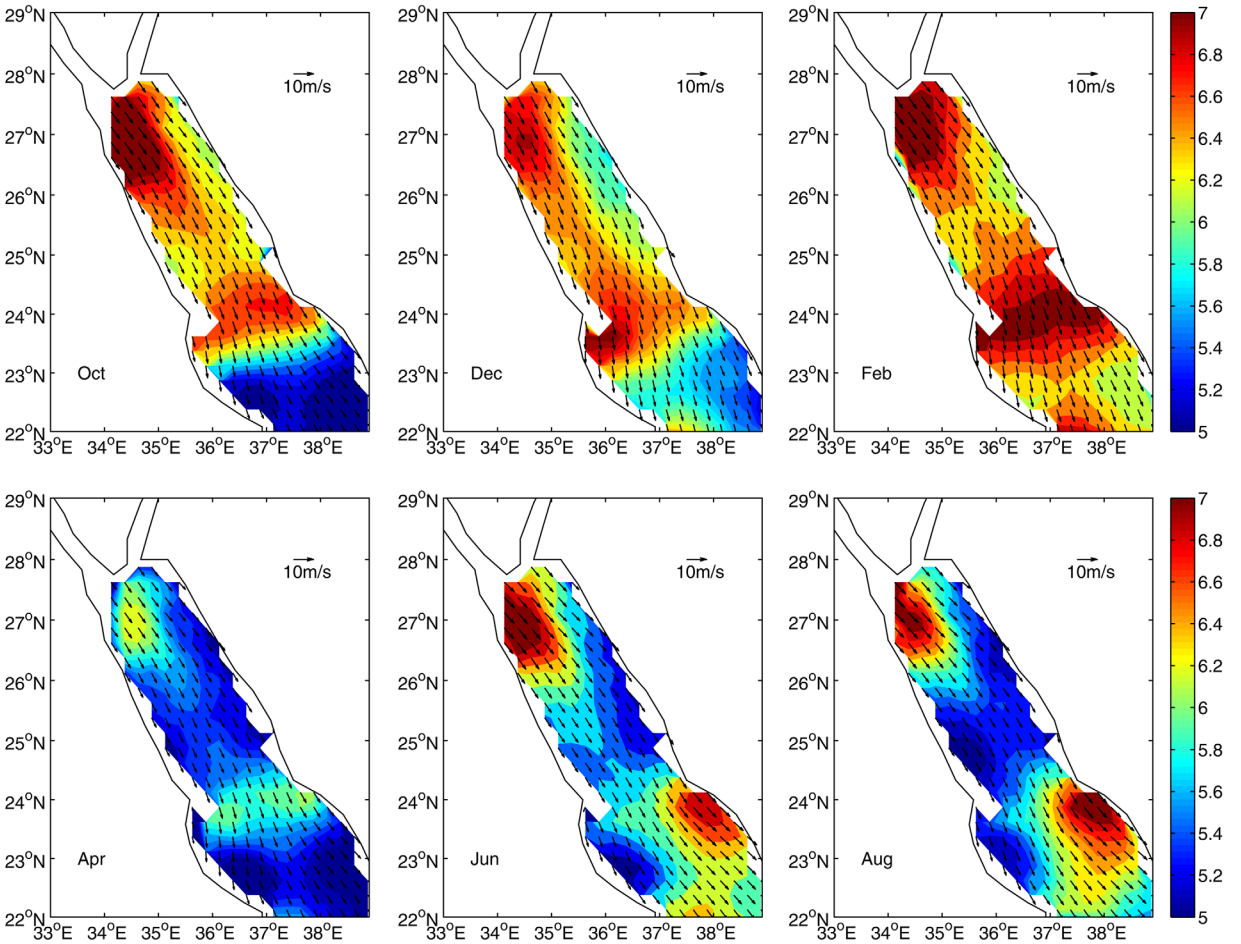

Figure 8. Monthly mean of 10 m wind vector field overlapped with its magnitude (colors) in selected months from QuikSCAT.

from the northern Red Sea to the southern Red Sea and the unselected sections show some repeated features. Discrete PV minima are found at a range of densities in these transects, from $\sigma_\theta = 27.3$–28.1 kg m^{-3}, with most common occurrence at $\sigma_\theta = 27.6$–28.1 kg m^{-3}. At transects 4 and 1, near the southern limit of the survey, no clear PV minimum layer is found. The March transects stopped at about 22°N, where transect 11 in September–October cruise is, so the low PV signal might have been missing in the southern Red Sea too in March 2010. Generally, the low PV layer in September–October 2011 is less identifiable than that in March 2010, and its density range appears to be broader. We choose a density range of $\sigma_\theta = 27.3$–28.1 kg m^{-3} to capture the main RSOW layer in September–October 2011. Much of the difference in the density range estimated from PV is likely due to restratification after winter mixing for 2011. This also might be because the RSOW layer is diluted by eddies and diapycnal mixing as RSOW moves southward after its formation in winter. The horizontal velocity measured by SADCP at 91 m depth in March 2010 and September–October 2011 shows that there are many eddies in the Red Sea (Figure 11).

Besides the PV minimum, transient tracers like CFCs and SF_6 can be used to study the spreading and the age of RSOW. In 2011 there is a CFC-12 maximum layer centered at about 150 m depth and a CFC-12 minimum layer centered at about 500 m depth (Figures 12 and 13). A similar structure is observed in the SF_6 distribution (Figure 14). Tracer concentrations are lower in the surface water than at 150 m because the temperature of the surface water is 5–6°C warmer and solubility is strongly dependent on and inversely related to temperature. Figure 14 shows that SF_6 is higher in surface water relative to the underlying RSOW than CFC-12 is. The primary reason is the difference in the atmospheric time histories (Figure 4) and hence input to surface water. SF_6 has continuously increased with time, but CFC-12 reached a maximum in the atmosphere and hence in surface water in about 2002. Thus, the water underlying the surface mixed layer

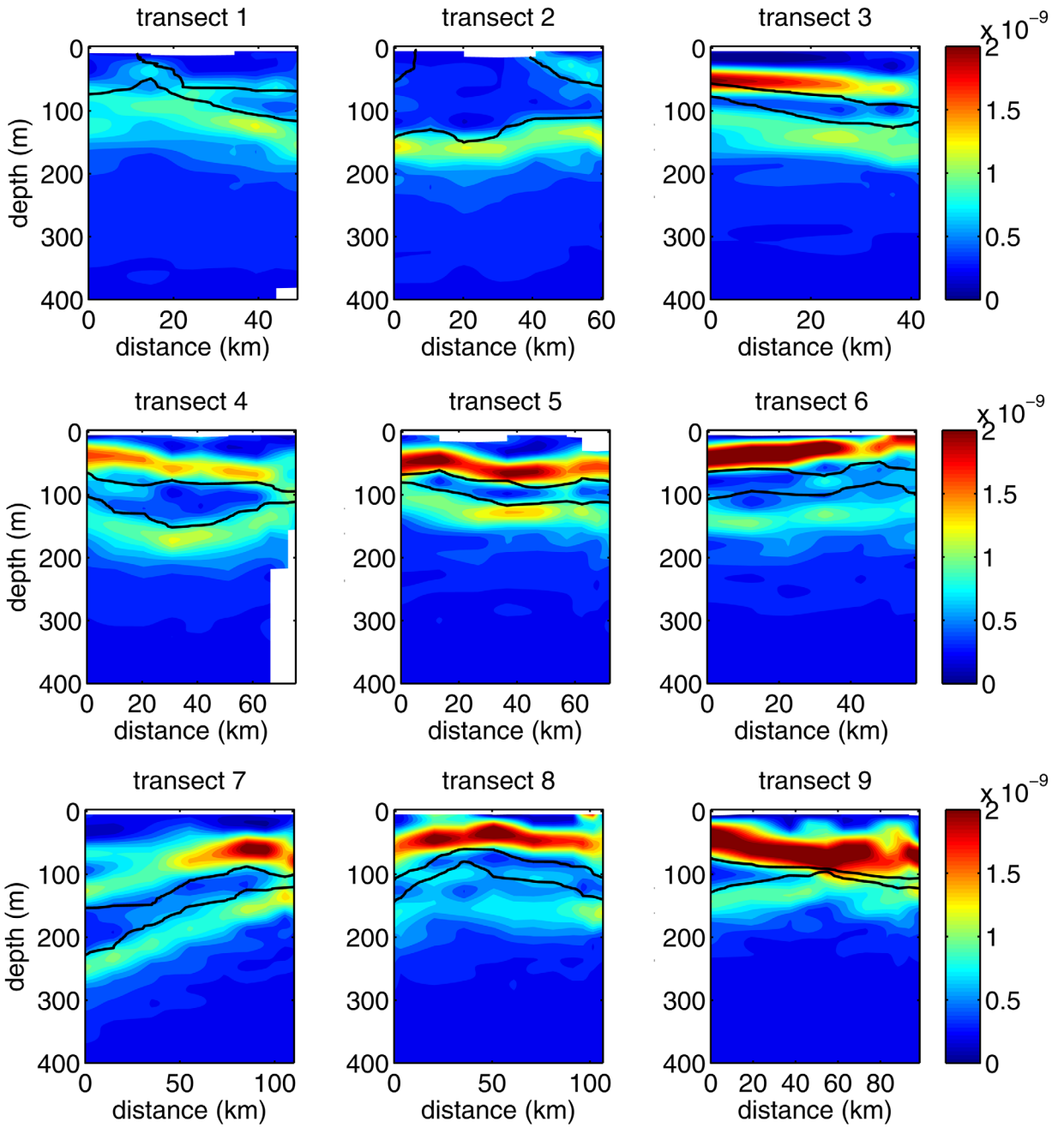

Figure 9. PV ($m^{-1}s^{-1}$) at nine transects during March 2010 cruise (see Figure 1 for locations). *x* axis is distance from the most west station. Isopycnals of 27.5 and 27.7 kg m^{-3} are plotted as solid black lines.

formed at a time when the CFC-12 was higher than it was in 2011 and the concentration in the underlying water is greater than in the surface water. Differences in solubility also have an impact. The solubility of SF_6 in seawater is less sensitive to temperature than that of CFC-12. For example, the solubility of CFC-12 in seawater with temperature of 29°C and salinity of 40 is 77% of the solubility in seawater with temperature of 23°C and salinity of 40, while the percentage is 82% for SF_6. The layer with maximum CFC-12 and SF_6 coincides with the minimum PV centered at about 150 m depth, and both are presumed to be signatures of recently ventilated RSOW. However, the high CFC-12 and SF_6 concentrations extend to deeper depths and densities than those defined by the PV minimum, presumably the result of convection and diapycnal mixing to deeper depths in previous years. The tongue of high CFC-12 and SF_6 centered at 150 m extends

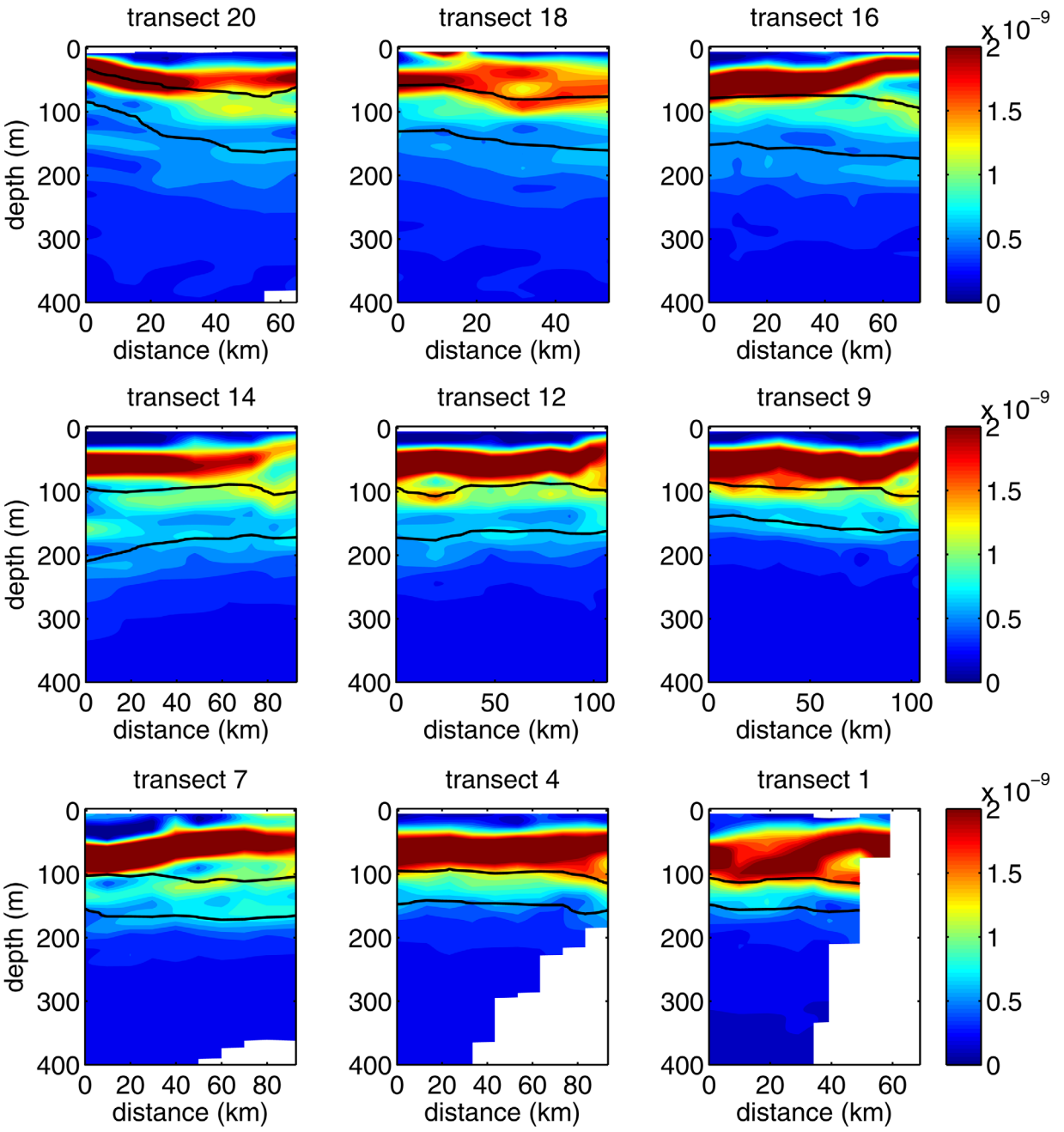

Figure 10. PV (m^{-1} s^{-1}) at nine selected transects during September–October 2011 cruise (see Figure 1 for locations). *x* axis is distance from the most west station. Isopycnals of 27.3 and 28.1 kg m^{-3} are plotted as solid black lines.

southward from the northern Red Sea, with decreasing concentration. This could be caused by mixing with older ambient water and older Gulf of Aden Intermediate Water, which intrudes over the Hanish Sill.

Evaporative cooling is primarily responsible for the formation of RSOW, but it is not easily identifiable as a subsurface salinity maximum within the Red Sea. This is because the underlying water mass, RSDW, is also high in salinity but has its source in dense outflows from the adjacent Gulfs of Suez and Aqaba [*Murray et al.*, 1984; *Cember*, 1988; *Woelk and Quadfasel*, 1996; *Plähn et al.*, 2002]. RSOW is identifiable as a salinity maximum downstream of the Red Sea in the Gulf of Aden [*Mecking and Warner*, 1999] and the northern Indian Ocean [*Beal et al.*, 2000], where it overlies fresher intermediate and deep Indian Ocean water masses.

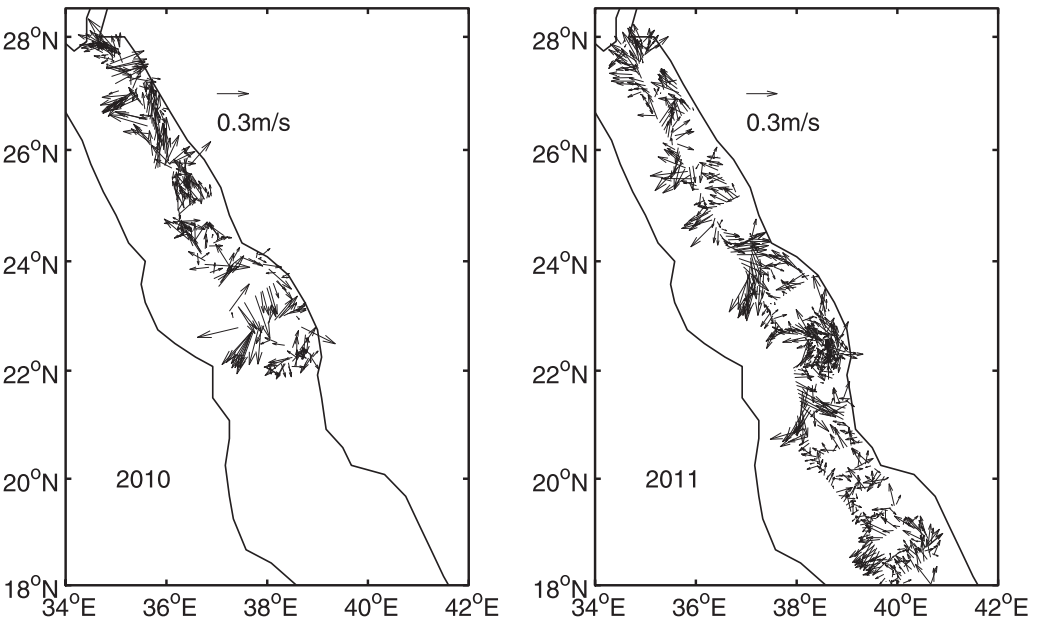

Figure 11. Horizontal velocity at 91 m depth, derived from the SADCP measurements in March 2010 and September–October 2011.

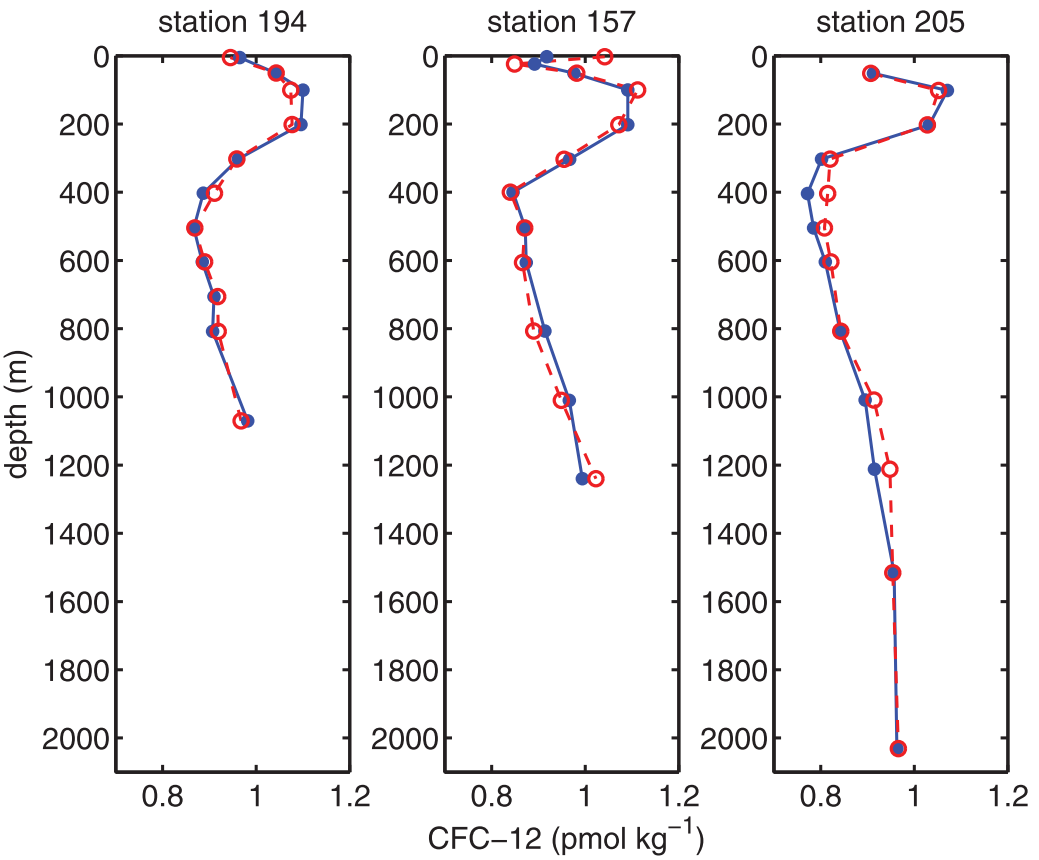

Figure 12. Vertical profiles of CFC-12 at three stations (see Figure 5 for station locations). Samples collected using stoppered bottles are plotted with blue dotted lines, while samples collected using ampoules are plotted with red circle lines. Agreement between the two methods is excellent.

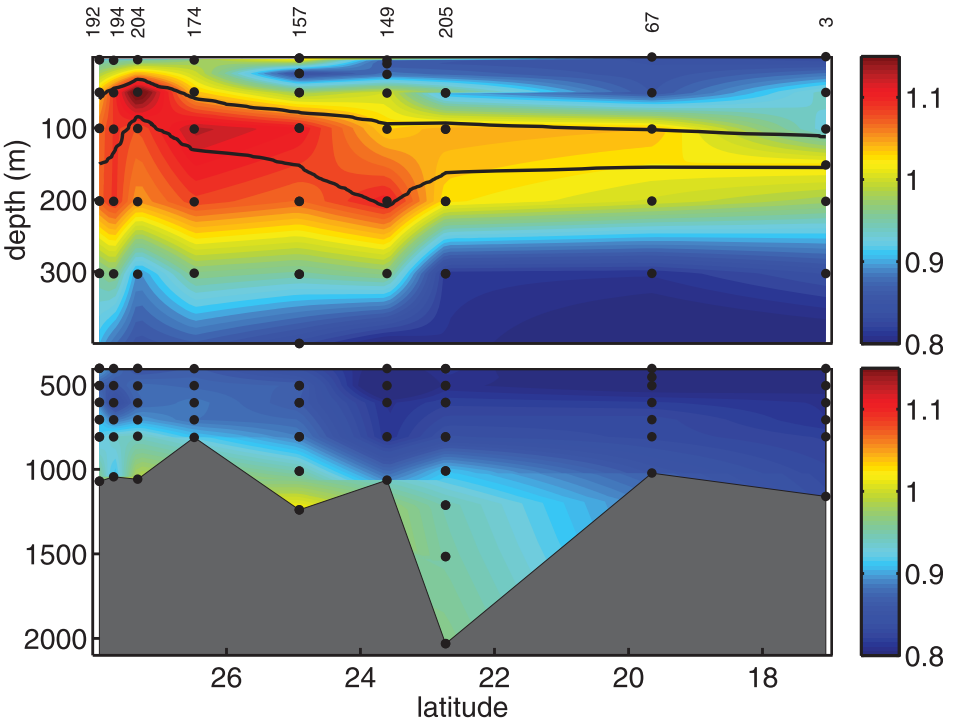

Figure 13. CFC-12 concentration (pmol kg^{-1}) along the central axis of the Red Sea (see Figure 5 for location). Station numbers and depth at which measurements were taken are marked with black dots. Isopycnals of 27.3 and 28.1 kg m^{-3} are plotted with black lines. Shaded area represents the bottom topography measured in September–October 2011 cruise. Note the change in depth scale between the top and bottom figures.

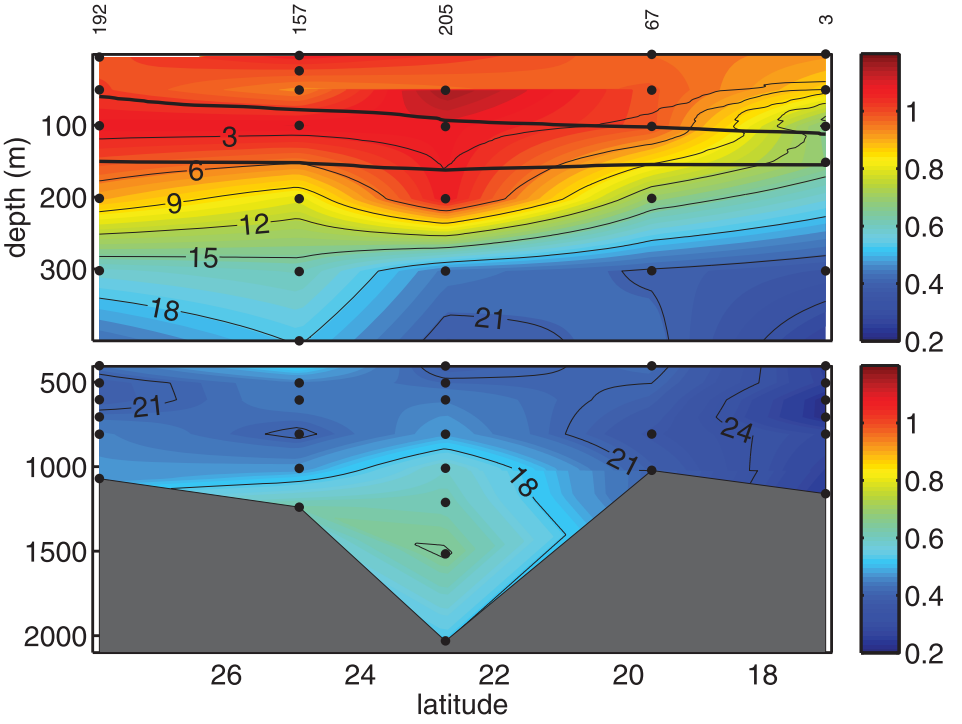

Figure 14. SF_6 concentration (colors, fmol kg^{-1}) and pSF6 age (years) (black contours) along the central axis of the Red Sea (see Figure 5 for location). Station numbers and depth at which measurements were taken are marked with black dots. Thick black lines indicate isopycnals of 27.3 and 28.1 kg m^{-3}. Shaded area represents the bottom topography measured on September–October 2011 cruise. Note the change in depth scale between top and bottom figures.

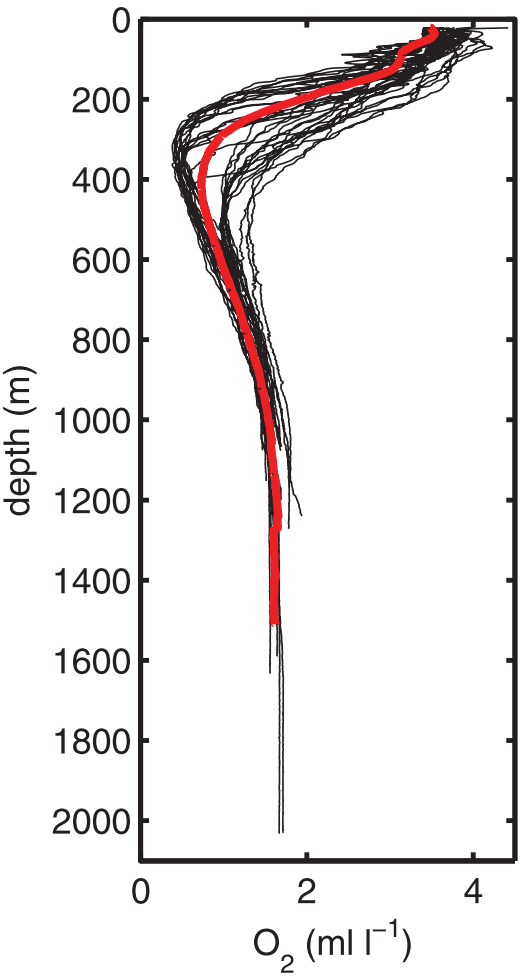

Figure 15. Vertical profiles of dissolved oxygen (mL L^{-1}) along the central axis of the Red Sea during the 2011 cruise (see Figure 1 for location). Thick red line represents mean vertical profile of dissolved oxygen averaged on all stations during the 2011 cruise.

In contrast, the CFC-12 and SF_6 concentrations continuously decrease from 200 to 500 m depth and then increase to the bottom of the Red Sea revealing the presence of recently ventilated RSDW. *Cember* [1988] observed essentially the same vertical structure for ^{14}C resulting from input of radiocarbon from nuclear weapons testing. There is now wide agreement between investigators that the source of the RSDW is from the Gulfs of Suez and Aqaba and that the open northern Red Sea is not likely a direct source of RSDW [*Murray et al.*, 1984; *Cember*, 1988; *Woelk and Quadfasel*, 1996; *Plähn et al.*, 2002]. Our CFC-12 and SF_6 observations lend further support to the notion that the deepening of mixed layer in wintertime in the northern Red Sea is not deep enough to ventilate the bottom layer of the Red Sea and that the bottom layer is ventilated by dense outflows from the Gulfs of Suez and Aqaba. The data also show for the first time the coincidence of low PV and high concentrations of the conservative transient tracers CFC-12 and SF_6, allowing the unambiguous identification of RSOW as far south as 17°N.

Oxygen enters seawater through air-sea interaction as does CFC-12 and SF_6. However, oxygen is not conservative and is produced by photosynthesis in the surface mixed layer and consumed by respiration beneath the mixed layer. Figure 15 shows vertical profiles of dissolved oxygen (O_2) concentration measured during the September–October 2011 cruise. As previously observed by *Sofianos and Johns* [2007], O_2 decreases from near surface water to about 400 m then increases in RSDW at the bottom. The vertical O_2 gradient decreases between 80 and 150 m, which coincides with the high CFC-12/SF_6 and low PV layer. However, there is no well-defined vertical maximum of O_2 in this layer as is the case for CFC-12/SF_6 due to oxygen consumption, demonstrating the advantage of CFC-12 and SF_6 as passive tracers in identifying RSOW.

Seawater ages were calculated from the SF_6 measurements. SF_6 concentrations in seawater were divided by the SF_6 solubility at in situ temperature and salinity [*Bullister et al.*, 2002] to determine pSF_6 (the atmospheric SF_6 partial pressure that is required to produce the observed seawater SF_6 concentration assuming equilibrium between the water and the atmosphere when the water was at the surface). The pSF_6 values were compared to the atmospheric time history of SF_6 (Figure 4; concentrations of CFC-12 and SF_6 in the atmosphere are available from http://cdiac.ornl.gov/oceans/new_atmCFC.html) to estimate the year of formation and age. This represents the mean age of each sample and is an estimate if the water parcel components formed within the past three decades when the SF_6 atmospheric concentration increased approximately linearly with time. The apparent uncertainty of ±15–20% on the SF_6 measurement results in an uncertainty of about ±2–3 years in the pSF_6 age. For the RSOW density horizon, the mean pSF_6 age is 2–4 years at the stations between the northern end of the Red Sea and 22°N (Figure 14). It then increases to about 15 years at station 3 (17°N), which is a result of transit time from the northern source region and mixing with older water in the southern Red Sea. This is in good agreement with the pCFC age of 12–13 years for RSOW measured in the Strait of Bab el Mandeb in 1995 [*Mecking and Warner*, 1999; *Rhein et al.*, 1997]. Older pCFC ages of 18–27 years were measured in RSOW in the western Gulf of Aden [*Mecking and Warner*, 1999].

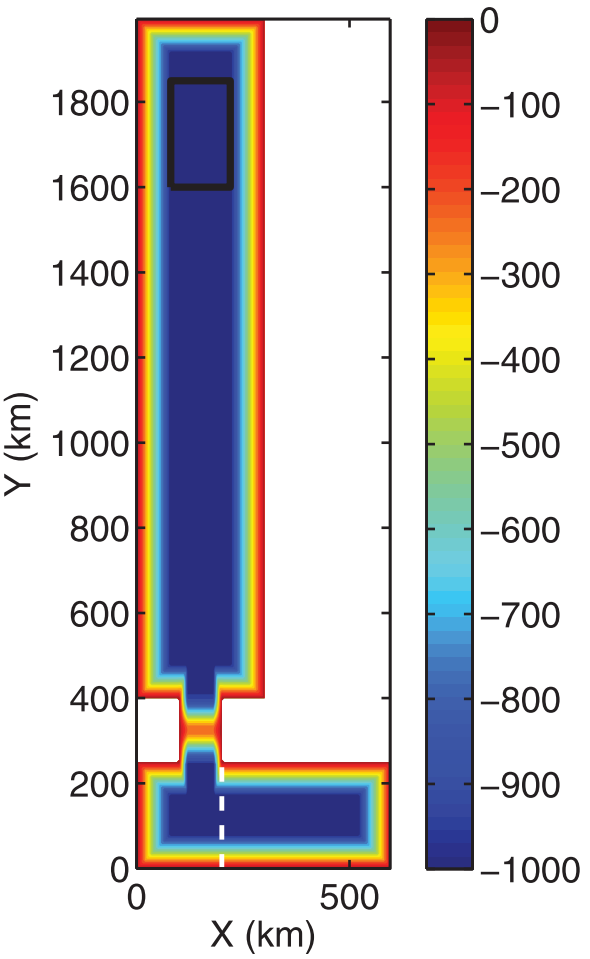

Figure 16. Model domain with bottom topography (colors, unit in m). Temperature and salinity are restored to the initial profiles in the region east of the dashed white line.

The overall mean age of RSOW within the Red Sea was estimated to be 6.9 years by integrating the pSF_6 age within RSOW layer along the Red Sea axis (Figure 14). Since there was not a station at the southern end of the Red Sea, the vertical pSF_6 age profile for station 3 was used at this location for the horizontal integration. The mean thickness of RSOW was determined by performing the same integration on the vertical distance between the density boundaries and was 62 m. The mean age of RSOW can also be calculated by dividing the volume of RSOW within the Red Sea by its rate of outflow to the Gulf of Aden. The area of the Red Sea is 438,000 km^2 and the estimated RSOW average thickness from above is 62 m, yielding a volume of 2.72×10^{13} m^3. The annual mean transport of RSOW to the Gulf of Aden was measured with current meters between 1995 and 1996 to be 0.36 Sv [*Sofianos et al.*, 2002]. The resulting age is 2.4 years. This age represents the mean residence time of water in the RSOW layer. However, the pSF_6 age is the mean time the water in RSOW has been isolated from the atmosphere. There are essentially two sources of RSOW: surface water within the Red Sea that mixes into the RSOW density layer, and subsurface water from the Gulf of Aden that flows into the Red Sea during summer [*Sofianos et al.*, 2002]. The Gulf of Aden water has been isolated from the atmosphere for a period of time prior to entering the Red Sea and thus pSF_6 and pCFC ages for RSOW will be greater than the mean residence time. *Rhein et al.* [1997] report the CFC-12 saturation for the Gulf of Aden inflow water immediately overlying RSOW in the Strait of Bab el Mandeb to be about 73% in 1995, which corresponds to a pCFC-12 age of 11 years. *Sofianos et al.* [2002] measured the annual inflow of Gulf of Aden water to be 0.07 Sv, which is 20% of the outflow of RSOW. This implies a mean relic or initial age of RSOW of 2.2 years prior to renewal by convection and vertical mixing; subtraction of this from the 6.9 years mean pSF_6 age yields a residence time of water in RSOW of 4.7 years. The tracer-based residence time is a roughly decadal integration and the transport-based residence time uses data for only 1 year. This might be the reason why the two estimations of residence time differ from each other.

5. Spreading of RSOW in an Idealized Numerical Experiment

5.1. Model Configuration

Since observations are limited in the Red Sea, numerical modeling is introduced to study the pathway and transit time of the RSOW from its formation region to the strait of Bab el Mandeb.

The Massachusetts Institute of Technology General Circulation Model (MITgcm) [*Marshall et al.*, 1997] is used to simulate the buoyancy-driven circulation in an idealized Red Sea and the trajectories of numerical particles. The model configuration is described in *Zhai et al.* [2015] (hereafter referred to as ZPB). The model domain includes the idealized Red Sea, Strait of Bab el Mandeb, and Gulf of Aden (Figure 16). The horizontal grid spacing is 5 km and there are 29 vertical levels, with thickness varying from 10 m at the surface to 100 m at the bottom.

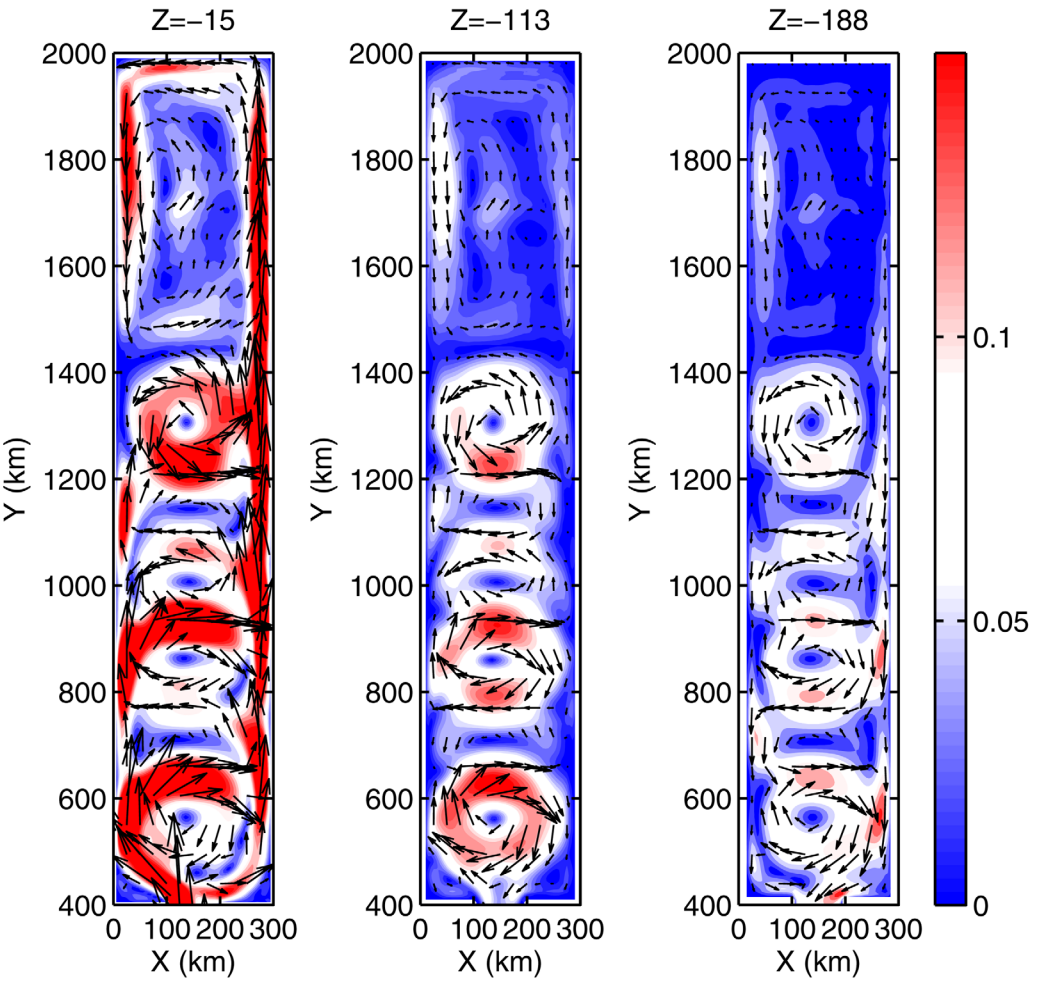

Figure 17. Five year mean horizontal velocity fields at depth of 15, 113, and 188 m. Color is velocity magnitude in m s^{-1}.

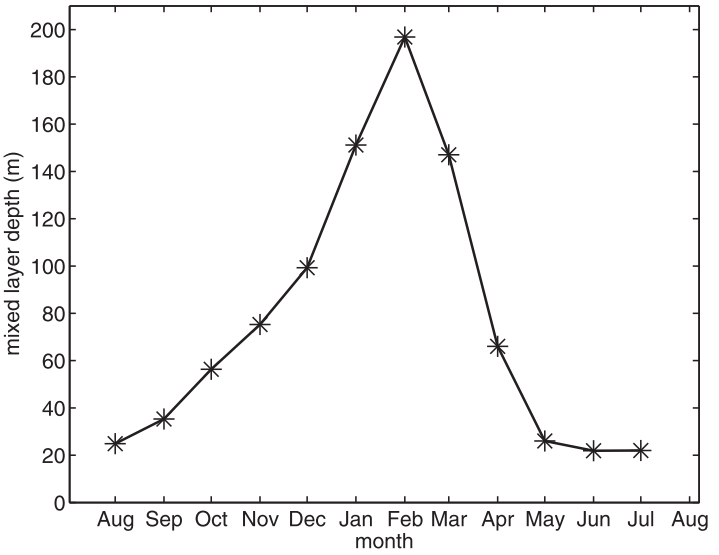

Figure 18. Time series of mixed-layer depth averaged in the black box shown in Figure 16.

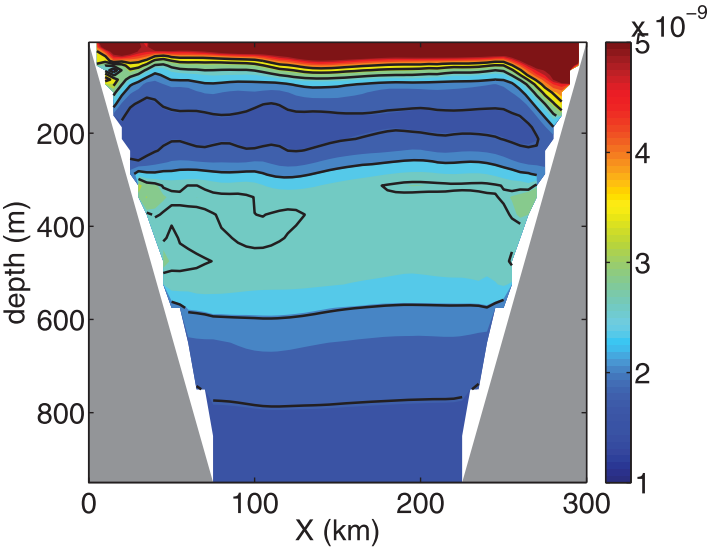

Figure 19. PV ($m^{-1}s^{-1}$) along Y = 1600 km in March.

The control numerical experiment in ZPB is forced by idealized surface buoyancy fluxes which increase linearly with latitude. The model in this study is forced by climatological monthly mean surface heat (*Q*) and freshwater (*E*) fluxes in the Red Sea. Monthly mean OAflux data from 1984 to 2009 was used to generate the climatological monthly mean sea surface fluxes. The annual mean *Q* and *E* over the Red Sea estimated using OAflux data are 19 W m^{-2} and 1.8 m yr^{-1}, which are close to estimations in *Sofianos et al*. [2002]. The zonally averaged 1° OAflux product in the Red Sea is linearly interpolated into the meridional grids in the model. The sea surface fluxes are zonally uniform in the model. The sea surface loses heat to the atmosphere in winter and absorbs heat from the atmosphere in summer. The freshwater flux to the atmosphere is positive all year round. Evaporation and heat loss in the northern Red Sea are stronger than in the southern Red Sea in winter. The model was run for 25 years with climatological monthly mean surface heat flux and evaporation. Based on the temporal evolution of temperature and kinetic energy within the Red Sea, the model reached a quasi-steady state after 10 years. Unless it is explicitly stated otherwise, the mean fields discussed in this study will be the average over the final 5 years of the 25 year simulation.

5.2. Model Results

The horizontal velocity fields averaged over the final 5 years at three levels are plotted in Figure 17. The cyclonic gyre in the northern Red Sea is centered at about Y = 1750 km. In the southern Red Sea, the circulation is dominated by a series of basin-scale eddies. The circulation in Figure 17 looks quite different from the model runs that appear in ZPB. That is because the surface buoyancy fluxes have different meridional structures in this study and in ZPB, as mentioned earlier in model configuration. Previous observational and modeling studies have suggested that eddies play an important role in the Red Sea circulation [*Morcos*, 1970; *Morcos and Soliman*, 1974; *Quadfasel and Baudner*, 1993; *Sofianos and Johns*, 2007]. Velocity measurements in March 2010 and September–October 2011 also reveal that there are many eddies in the Red Sea (Figure 11). Observations shown in section 3 suggest that RSOW is formed through mixed-layer deepening in winter. The seasonal variation of mixed-layer depth is simulated in the numerical model (Figure 18). Mixed-layer depth is defined as the depth at which potential density is different from the density at 10 m depth by 0.06 kg m^{-3}. In the numerical model, mixed-layer depth reaches about 200 m in February. In observations, the RSOW is identified as a layer with low PV. The numerical model also presents the same feature. Figure 19 plots PV along Y = 1600 km in the numerical model in March. There is a low PV layer centered at 200 m below the surface, which is the RSOW layer in the numerical model.

In order to investigate the pathway of RSOW through the Red Sea, backward trajectories of particles that enter the strait from the north are calculated, using 2 years of three-dimensional velocity fields from the numerical model as input. The time interval of velocity fields is 5 days. The time step in the trajectory calculation is 3 h. The 5 day velocity fields are linearly interpolated into 3 h time scale in the calculation. The particles are released every 5 days for 2 years at the strait and the trajectories are integrated over 10 years. 20×15×144=43200 particles are released, where 20 represents number of zonal grids at the strait, 15 represents the number of vertical levels at the strait and 144 represents the total number of particles at each grid point that are released in 2 years. Since the backward trajectories are integrated over 10 years, the 2 year velocity fields are recycled five times. This approach is similar to that of *van Sebille et al*. [2013] in which

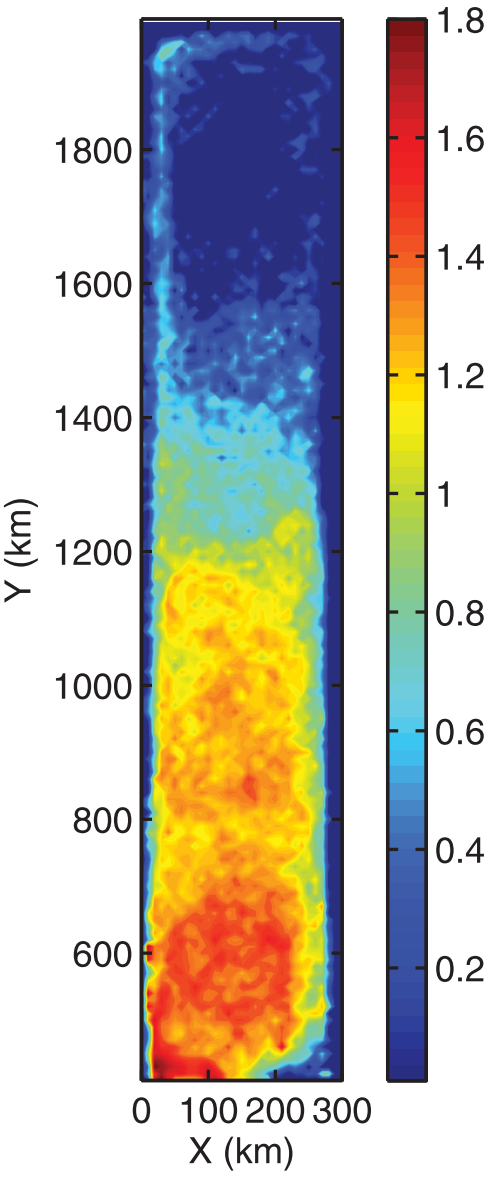

Figure 20. The pathway of RSOW before entering the strait. The particles are released at the strait at the depths of the outflowing RSOW and tracked backward in time. The map shows the percentage ($\log_{10}$(percentage)) of particles that cross through each 10 km×10 km cell at some time in the 10 year integration summing over the RSOW layer.

the pathways of the Antarctic Bottom Water were diagnosed. In our calculation, only particles at the RSOW density range are considered.

Using the backward trajectories of particles, the probability map of RSOW particles is produced (Figure 20). The probability can be interpreted as the chance that a particle will visit that grid point within 10 years. Thus, the probability map is a different expression of pathways. The probability shown in Figure 20 is the sum of probability in the RSOW layer.

From the probability map, it is indicated that in the southern Red Sea, instead of moving along the boundary current, the RSOW particles recirculate before they enter the Strait of Bab el Mandeb. In the northern Red Sea, the probability is higher along the western boundary than along the eastern boundary. This indicates that most of the particles flow southward along the western boundary in the northern Red Sea on their way to the strait from the formation region. The different horizontal structures of the probability map in the southern and northern Red Sea can be explained by the horizontal velocity fields in Figure 17. The velocity fields in the northern Red Sea are much simpler than that in the southern Red Sea. North of 1400 km, there is a strong western boundary current penetrating to 188 m. Because of the influence of eddies, the probability in the southern Red Sea is nearly homogeneous.

In order to estimate the transit time of RSOW from the formation region to the strait, particles within the RSOW layer north of y = 1500 km are released every 5 days for 2 years at each grid point in the model. Therefore, at each grid point, 144 particles are released in 2 years and the model is run for 20 years. The time when a particle crosses the strait is recorded as transit time. The transit time distribution (TTD) indicates that the transit time for particles ranges from 0.5 to 16 years, the dominant transit time is about 3 years and the mean transit time is about 4.8 years (Figure 21). This mean transit time is equivalent to the residence time and is of the right order compared to the residence time estimates of 2.4 and 4.7 years made earlier.

6. Conclusions and Discussion

In this study, we have analyzed air-sea fluxes, hydrographic data, and satellite SST images, and find that the RSOW is formed by mixed-layer deepening in wintertime caused by sea surface buoyancy loss in the northern Red Sea. Hydrographic and transient tracer data measured in March 2010 and September–October 2011 suggest that the winter surface mixed-layer deepening due to convection and mixing in the northern Red Sea is confined to the upper layer with potential density smaller than about 28.1 kg m^{-3}. This implies that buoyancy loss in the northern Red Sea was not strong enough to generate deep convection that extends to the bottom, as also discussed in several earlier studies. Recently ventilated water of

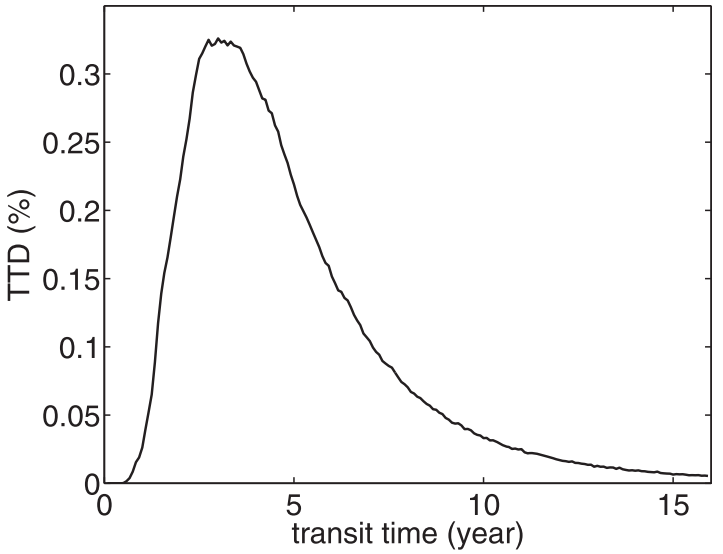

Figure 21. Transit time distribution (TTD) for particles released north of y = 1500 km in the RSOW layer.

sufficient density to sink to the bottom does enter the northern Red Sea from the Gulfs of Suez and Aqaba to form RSDW and the winter surface mixed-layer deepening, which generally does not exceed 200 m, forms RSOW.

RSOW is identified as a minimum in PV due to weak stratification and as a maximum in CFC-12 and SF_6 due to ventilation of the RSOW layer during formation. This study provides new evidence of the horizontal and vertical structure of RSOW spreading. RSOW spreads southward after its formation in the northern Red Sea. The density range of the RSOW in September–October 2011 is broader than that in March 2010 (Figures 9 and 10). This might be because the RSOW layer is diluted by eddies and diapycnal mixing while it moves southward. Interannual variability of atmospheric forcing may also cause the density differences.

Numerical model results indicate that RSOW flows southward along the western boundary in the northern Red Sea in a strong western boundary current. However, there are many basin-scale eddies in the southern Red Sea. As a result, RSOW circulates throughout the southern basin instead of being confined in a boundary current and this increases the time water parcels spend in the southern Red Sea relative to the northern Red Sea. The dominant transit time of the RSOW particles from the formation region to the exit at the strait is about 3 years and the mean transit time (equivalent to the residence time) is about 4.8 years. This is larger than the RSOW residence time estimated from the annual mean transport measured at the Strait of Bab el Mandeb and the total volume of RSOW inside the Red Sea, 2.4 years, but in excellent agreement with the residence time estimated from pSF_6 and pCFC-12 ages, 4.7 years. The pSF_6 age indicates that the mean age of seawater within the RSOW layer increases from 2 to 4 years in the northern Red Sea to about 15 years at 17°N. SF_6 has entered the atmosphere since the 1960s and the pSF_6 age represents a mean value of mixtures of water formed over the past three decades. The older age in the southern Red Sea is the result of mixing between recently formed RSOW with older vintages of RSOW and with older water flowing into the Red Sea from the Gulf of Aden. This is consistent with the model circulation which shows RSOW formed in the northern Red Sea rapidly transported to the southern Red Sea where it becomes incorporated in long flow paths generated by the large number of basin-scale eddies before exiting through the strait, which results in older ages for the water.

Numerical modeling in this study is very idealized and is not intended to resolve the actual Red Sea circulation, but to explore some features of the spreading of RSOW in the Red Sea. Further observations and realistic numerical modeling with particle tracking and tracers such as SF_6 are needed to investigate the spreading pathway of RSOW in more detail.

Acknowledgments
Hydrographic and CFC-12/SF_6 data can be accessed from authors. Other data used in this study are available in the following websites: sea surface temperature data at http://www.remss.com/measurements/sea-surface-temperature, Sea Surface Heat Flux at http://oaflux.whoi.edu/data.html, QuikSCAT wind data at http://www.remss.com/missions/qscat, and ASCAT wind data at http://www.remss.com/missions/ascat. This work is supported by award (USA 00002, KSA 00011, and KSA 00011/02) made by King Abdullah University of Science and Technology (KAUST), National Science Foundation (OCE0927017), and WHOI Academic Program Office. We thank E. Gorman for measurement of the CFC-12 and SF_6 samples. We thank Yasser Abualnaja, Elizabeth Bonk, Marshall Swartz, and Marti Jeglinski for helping with sampling of CFC-12 and SF_6. We also thank two anonymous reviewers for their thoughtful and helpful reviews.

References

Beal, L. M., A. Ffield, and A. L. Gordon (2000), Spreading of Red Sea overflow waters in the Indian Ocean, *J. Geophys. Res.*, *105*(C4), 8549–8564.
Bentamy, A., D. Croize-Fillon, and C. Perigaud (2008), Characterization of ASCAT measurements based on buoy and QuikSCAT wind vector observations, *Ocean Sci.*, *4*, 265–274.
Bower, A. S., and H. H. Furey (2011), Mesoscale eddies in the Gulf of Aden and their impact on the spreading of Red Sea Outflow Water, *Prog. Oceanogr.*, *96*, 14–39, doi:10.1016/j.pocean.2011.09.003.
Bower, A. S., H. D. Hunt, and J. F. Price (2000), Character and dynamics of the Red Sea and Persian Gulf outflows, *J. Geophys. Res.*, *105*(C3), 6387–6414.
Bower, A. S., W. E. Johns, D. M. Fratantoni, and H. Peters (2005), Equilibration and circulation of Red Sea Outflow Water in the Western Gulf of Aden, *J. Phys. Oceanogr.*, *35*, 1963–1985.
Bullister, J. K., D. P. Wisegarver, and F. A. Menzia (2002), The solubility of sulfur hexafluoride in water and seawater, *Deep Sea Res., Part I*, *49*, 175–187.
Cember, R. P. (1988), On the sources, formation, and circulation of Red-Sea deep-water, *J. Geophys. Res.*, *93*(C7), 8175–8191.
Chen, C., et al. (2014), Process modeling studies of physical mechanisms of the formation of an anticyclonic eddy in the central Red Sea, *J. Geophys. Res. Oceans*, *119*, 1445–1464, doi:10.1002/2013JC009351.
Clifford, M., C. Horton, J. Schmitz, and L. H. Kantha (1997), An oceanographic nowcast/forecast system for the Red Sea, *J. Geophys. Res.*, *102*(C11), 25,101–25,122.
Fine, R. A., W. M. Smethie Jr., J. L. Bullister, M. Rhein, D.-H. Min, M. J. Warner, A. Poisson, and R. F. Weiss (2008), Decadal ventilation and mixing of Indian Ocean waters, *Deep Sea Res., Part I*, *55*, 20–37.
Gordon, A. L., J. R. E. Lutjeharms, and M. L. Grundlingh (1987), Stratification and circulation at the Agulhas Retroflection, *Deep Sea Res., Part A*, *34*, 565–599.
Hanawa, K., and L. D. Talley (2001), Mode waters, in *Ocean Circulation and Climate*, edited by G. Siedler and J. Church, pp. 373–386, Academic, New York.
Hartin, C. A., R. A. Fine, B. M. Sloyan, L. D. Talley, T. K. Chereskin, and J. Happell (2011), Formation rates of subantarctic mode water and antarctic intermediate water within the south pacific, *Deep Sea Res., Part I*, *58*(5), 524–534.
Jiang, H., J. T. Farrar, R. C. Beardsley, R. Chen, and C. Chen (2009), Zonal surface wind jets across the Red Sea due to mountain gap forcing along both sides of the Red Sea, *Geophys. Res. Lett.*, *36*, L19605, doi:10.1029/2009GL040008.
Maillard, C., and G. Soliman (1986), Hydrography of the Red Sea and exchanges with the Indian Ocean in summer, *Oceanol. Acta*, *9*, 249–269.
Manasrah, R., M. Badran, H. U. Lass, and W. Fennel (2004), Circulation and winter deep-water formation in the northern Red Sea, *Oceanologia*, *46*(1), 5–23.
Marshall, J., C. Hill, L. Perelman, and A. Adcroft (1997), Hydrostatic, quasi-hydrostatic, and nonhydrostatic ocean modeling, *J. Geophys. Res.*, *102*(C3), 5733–5752.
Mecking, S., and M. J. Warner (1999), Ventilation of Red Sea Water with respect to chlorofluorocarbons, *J. Geophys. Res.*, *104*(C5), 11,087–11,098.
Mecking, S., and M. J. Warner (2001), On the subsurface CFC maxima in the subtropical North Pacific thermocline and their relation to mode waters and oxygen maxima, *J. Geophys. Res.*, *106*(C10), 22,179–22,198.
Mensch, M., W. M. Smethie Jr., P. Schlosser, R. Weppernig, and R. Bayer (1998), Transient tracer observations from the western Weddell Sea during the drift and recovery of Ice Station Weddell, in *Ocean, Ice and Atmosphere: Interactions at the Antarctic Continental Margin*, edited by S. S. Jacobs and R. F. Weiss, pp. 241–256, AGU, Washington, D. C.
Morcos, S. (1970), Physical and chemical oceanography of the Red Sea, *Oceanogr. Mar. Biol.*, *8*, 73–202.
Morcos, S., and G. F. Soliman (1974), Circulation and deep water formation in the northern Red Sea in winter, in *L'oceanographic Physique de la Mer Rouge*, pp. 91–103, The Centre National pour l'Exploration des Oceans (CNEXO), Paris.
Murray, S. P., and W. Johns (1997), Direct observations of seasonal exchange through the Bab el Mandeb Strait, *Geophys. Res. Lett.*, *24*(21), 2557–2560.
Murray, S. P., A. Hecht, and A. Babcock (1984), On the mean flow in the Tiran Strait in winter, *J. Mar. Res.*, *42*, 265–284.
Neumann, A. C., and D. A. McGill (1962), Circulation of the Red Sea in early summer, *Deep Sea Res. Oceanogr. Abstr.*, *8*, 223–235.
Papadopoulos, V. P., Y. Abualnaja, S. A. Josey, A. Bower, D. E. Raitsos, H. Kontoyiannis, and I. Hoteit (2013), Atmospheric forcing of the winter air–sea heat fluxes over the northern Red Sea, *J. Clim.*, *26*, 1685–1701.
Patzert, W. C. (1974), Volume and heat transports between the Red Sea and Gulf of Aden, notes on the Red Sea heat budget, in *L'oceanographie Physique de la Mer Rouge*, pp. 191–201, The Centre National pour l'Exploration des Oceans (CNEXO), Paris.
Phillips, O. M. (1966), On turbulent convection currents and the circulation of the Red Sea, *Deep Sea Res. Oceanogr. Abstr.*, *13*, 1149–1160.
Plähn, O., B. Baschek, T. H. Badewien, M. Walter, and M. Rhein (2002), Importance of the Gulf of Aqaba for the formation of bottom water in the Red Sea, *J. Geophys. Res.*, *107*(C8), 3108, doi:10.1029/2000JC000342.
Quadfasel, D., and H. Baudner (1993), Gyre-scale circulation cells in the Red-Se, *Oceanol. Acta*, *16*(3), 221–229.
Rhein, M., L. Stramma, and O. Plahn (1997), Tracer studies of the intermediate layer of the Arabian Sea, *Geophys. Res. Lett.*, *24*(21), 2561–2564.
Schlosser, P., J. L. Bullister, and R. Bayer (1991), Studies of deep water formation and circulation in the Weddell Sea using natural and anthropogenic tracers, *Mar. Chem.*, *35*, 97–122.
Smeed, D. A. (2004), Exchange through the Bab el Mandab, *Deep Sea Res., Part II*, *51*, 455–474.
Smethie, W. M., Jr. (1993), Tracing the thermohaline circulation in the western North Atlantic using chlorofluorocarbons, *Prog. Oceanogr.*, *31*, 51–99.
Smethie, W. M., Jr., R. A. Fine, and E. P. Jones (2000), Tracing the flow of North Atlantic Deep Water using chlorofluorocarbons, *J. Geophys. Res.*, *105*(C6), 14,297–14,323.
Sofianos, S. S., and W. E. Johns (2003), An oceanic general circulation model (OGCM) investigation of the Red Sea circulation: 2. Three-dimensional circulation in the Red Sea, *J. Geophys. Res.*, *108*(C3), 3066, doi:10.1029/2001JC001185.
Sofianos, S. S., and W. E. Johns (2007), Observations of the summer Red Sea circulation, *J. Geophys. Res.*, *112*, C06025, doi:10.1029/2006JC003886.
Sofianos, S. S., W. E. Johns, and S. P. Murray (2002), Heat and freshwater budgets in the Red Sea from direct observations at Bab el Mandeb, *Deep Sea Res., Part II*, *49*, 1323–1340.

Valentine, H. R., J. R. E. Lutjeharms, and G. B. Brundrit (1993), The water masses and volumetry of the southern Agulhas Current region, *Deep Sea Res., Part I*, *40*, 1285–1305.

van Sebille, E., P. Spence, M. R. Mazloff, M. H. England, S. R. Rintoul, and O. A. Saenko (2013), Abyssal connections of Antarctic Bottom Water in a southern ocean state estimate, *Geophys. Res. Lett.*, *40*, 2177–2182, doi:10.1002/grl.50483.

Warner, M. J., and R. F. Weiss (1985), Solubilities of chlorofluorocarbons 11 and 12 in water and seawater, *Deep Sea Res., Part A*, *32*, 1485–1497.

Willey, D. A., R. A. Fine, R. E. Sonnerup, J. L. Bullister, W. M. Smethie Jr., and M. J. Warner (2004), Global oceanic chlorofluorocarbon inventory, *Geophys. Res. Lett.*, *31*, L01303, doi:10.1029/2003GL018816.

Woelk, S., and D. Quadfasel (1996), Renewal of deep water in the Red Sea during 1982–1987, *J. Geophys. Res.*, *101*(C8), 18,155–18,165.

Wyrtki, K. (1973), Physical oceanography of the Indian Ocean, in *Ecological Studies—Analysis and Synthesis*, edited by B. Zeitzschel, and S. A. Gerlach, vol. 3, pp. 18–36, Springer, Berlin.

Yao, F., I. Hoteit, L. Pratt, A. Bower, A. Kohl, G. Gopalakrishnan, and D. Rivas (2014), Seasonal overturning circulation in the Red Sea: 2. Winter circulation, *J. Geophys. Res. Oceans*, *119*, 2263–2289, doi:10.1002/2013JC009004.

Yu, L., X. Jin, and R. A. Weller (2008), Multidecade global flux datasets from the objectively analyzed air-sea fluxes (OAFlux) project: Latent and sensible heat fluxes, ocean evaporation, and related surface meteorological variables, *Tech. Rep. OA-2008-01*, 64 pp., Woods Hole Oceanogr. Inst., Woods Hole, Mass.

Zhai, P., and A. S. Bower (2013), The response of the Red Sea to a strong wind jet near the Tokar Gap in summer, *J. Geophys. Res. Oceans*, *118*, 422–434, doi:10.1029/2012JC008444.

Zhai, P., L. J. Pratt, and A. Bower (2015), On the crossover of boundary currents in an idealized model of the Red Sea, *J. Phys. Oceanogr.*, *45*, 1410–1425.